0830-L-02
NAS 1.29/3-2:99-01

NASA Tech Briefs

National Aeronautics and
Space Administration



Electronic Components and Circuits



Electronic Systems



Physical Sciences



Materials



Computer Programs



Mechanics



Machinery



Fabrication Technology



Mathematics and Information Sciences



Life Sciences

COMPLETED

99-01

January 1999

CA 9901238

INTRODUCTION

Tech Briefs are short announcements of new technology derived from the research and development activities of the National Aeronautics and Space Administration. These Briefs emphasize information considered likely to be transferable across industrial, regional, or disciplinary lines and are issued to encourage commercial application.

Availability of NASA Tech Briefs and TSP's

Distribution of NASA Tech Briefs, a monthly periodical publication, is limited to engineers in U.S. Industry and to other domestic technology transfer agents. Requests for individual Tech Briefs or for Technical Support Packages (TSP's) announced herein should be addressed to

NASA Center for AeroSpace Information
Technology Transfer Office
800 Elkridge Landing Rd.
Linthicum Heights, MD 21090-2934
Telephone No. (301) 621-0245

Please reference the three-letter, five-digit control number located at the end of each Tech Brief. Information on NASA's Technology Utilization Program, its documents, and services is also available at the same facility.

Technology Utilization Officers and Patent Counsels are located at NASA field installations to provide technology-transfer access to industrial users. Inquiries can be made by writing to NASA field installations listed below.

Technology Utilization Officers and Patent Counsels

Ames Research Center
Technology Utilization Officer
Mail Code 223-3
Moffett Field, CA 94035

Patent Counsel
Mail Code 200-11
Moffett Field, CA 94035

Goddard Space Flight Center
Technology Utilization Officer
Mail Code 702-1
Greenbelt, MD 20771

Patent Counsel
Mail Code 204
Greenbelt, MD 20771

Lyndon B. Johnson Space Center
Technology Utilization Officer
Mail Code IC-4
Houston, TX 77058

Patent Counsel
Mail Code AL3
Houston, TX 77058

John F. Kennedy Space Center
Technology Utilization Officer
Mail Stop PT-PMO-A
Kennedy Space Center, FL 32899

Patent Counsel
Mail Code PT-PAT
Kennedy Space Center, FL 32899

Langley Research Center
Technology Utilization Officer
Mail Stop 143
Hampton, VA 23665

Patent Counsel
Mail Code 279
Hampton, VA 23665

Lewis Research Center
Technology Utilization Officer
Mail Stop 7-3
21000 Brookpark Road
Cleveland, OH 44135

Patent Counsel
Mail Code LE-LAW
21000 Brookpark Road
Cleveland, OH 44135

Jet Propulsion Laboratory
Technology Utilization Officer
Mail Stop 156-211
4800 Oak Grove Drive
Pasadena, CA 91109

NASA Resident Office-JPL
Technology Utilization Officer
Mail Stop 180-801
4800 Oak Grove Drive
Pasadena, CA 91109

Patent Counsel
Mail Code 180-801
4800 Oak Grove Drive
Pasadena, CA 91109

George C. Marshall Space Flight Center
Technology Utilization Officer
Code AT01
Marshall Space Flight Center, AL 35812

Patent Counsel
Mail Code CC01
Marshall Space Flight Center, AL 35812

John C. Stennis Space Center
Technology Utilization Officer
Code HA-30
Stennis Space Center, MS 39529

NASA Headquarters
Technology Utilization Officer
Code CU
Washington, DC 20546

Assistant General Counsel for Patent Matters
Code GP
Washington, DC 20546

Dryden Flight Research Center
Technology Utilization Officer
M/S D21-31
Bldg. 4832 Whse 7
Lilly Dr.
Edwards, CA 93523

BLANK PAGE

NASA TechBriefs

National Aeronautics and
Space Administration

January 1999
99-01

5 Electronic Components and Circuits

13 Electronic Systems

17 Physical Sciences

27 Materials

33 Computer Programs

37 Mechanics

43 Machinery

47 Mathematics and Information Sciences

51 Life Sciences

This document was prepared under the sponsorship of the National Aeronautics and Space Administration. Neither the United States Government nor any person acting on behalf of the United States Government assumes any liability resulting from the use of the information contained in this document, or warrants that such use will be free from privately owned rights.

BLANK PAGE



Electronic Components and Circuits

Hardware, Techniques, and Processes

7 High-Efficiency, Long-Life Pulsed Inductive Plasma Thrusters
8 Solar-Cell System With High Conversion Efficiency
9 Packaging Electronic Circuits in Multi-Board Modules
9 Dual-Function Microelectronic Sensors
10 Luneberg Lenses Made of Open-Cell Polyurethane Foams

BLANK PAGE

High-Efficiency, Long-Life Pulsed Inductive Plasma Thrusters

Advanced pulse circuits deliver optimally shaped pulses and recover reflected energy.

Lewis Research Center, Cleveland, Ohio

Improved pulsed inductive plasma accelerators are undergoing development for use as long-life thrusters for propulsion of spacecraft on interplanetary missions and for maneuvering of spacecraft in orbit around the Earth. On Earth, plasma accelerators of this type could be used to produce a variety of atomic, molecular, and plasma beams for scientific experimentation and industrial processing (especially processing of materials in the fabrication of microcircuits). The principal advantages of the developmental accelerators over older pulsed inductive plasma accelerators arise from the use of advanced solid-state electronic pulse circuits, which operate at high repetition rates (as much as a couple of kilohertz), have long operating lives (10^{11} shots), deliver optimally shaped pulses, and recover reflected energy.

Some discussion of pulsed inductive plasma accelerators in general is prerequisite to a meaningful description of the present improved design concept. Figure 1 illustrates the basic principle of operation. A short pulse of electric current is sent through the coil by closing an electronic switch between a coil and a previously charged capacitor bank. The rapid rise of the axial magnetic field produces an azimuthal electric field, which electrically breaks down a propellant gas in a chamber adjacent to the coil, creating a plasma current ring in the direction opposite that of the current in the coil. The magnetic repulsion between the currents in the coil and the plasma drives the plasma away from the coil.

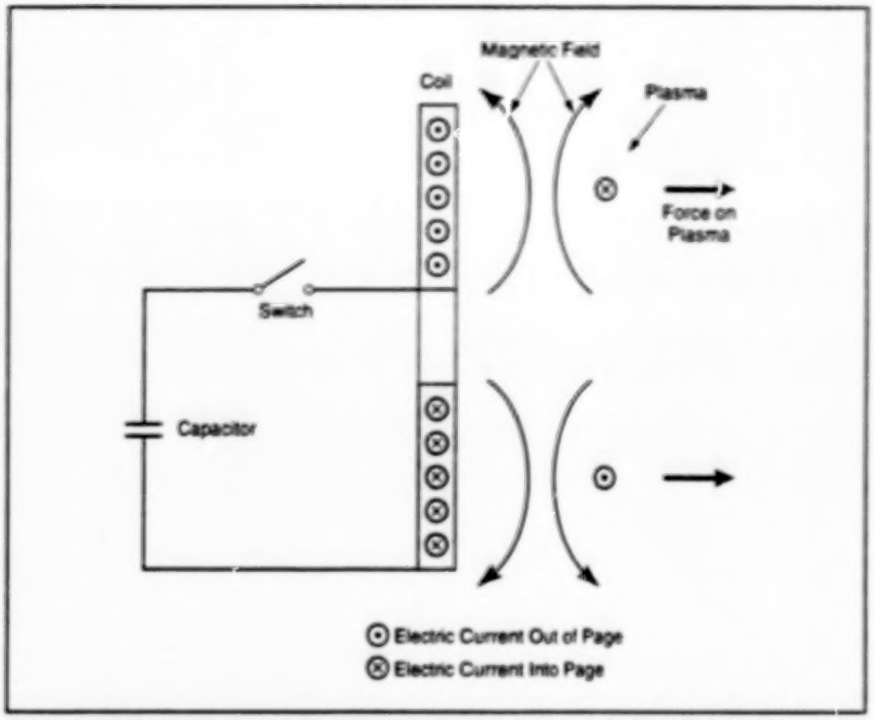


Figure 1. The **Pulsed Current in the Coil** generates a pulsed magnetic field that induces an opposing current in the plasma, with resultant magnetic force that pushes the plasma away from the coil.

Pulsed inductive plasma accelerators offer advantages over electric plasma accelerators, in which electrodes supply currents to form the plasmas. Erosion of electrodes severely limits operational lifetimes and introduces electrode atoms into the plasmas. In the case of a plasma for industrial processing or scientific experimentation, contamination with electrode material can be unacceptable. Because a pulsed inductive plasma accelerator operates without electrodes and the plasma is pushed away out of contact with the induction coil immediately upon formation, there is much less erosion, and the plasma is much cleaner than in an electric plasma accelerator.

Until now, the performances of pulsed inductive plasma accelerators have been constrained by the unavailability of reli-

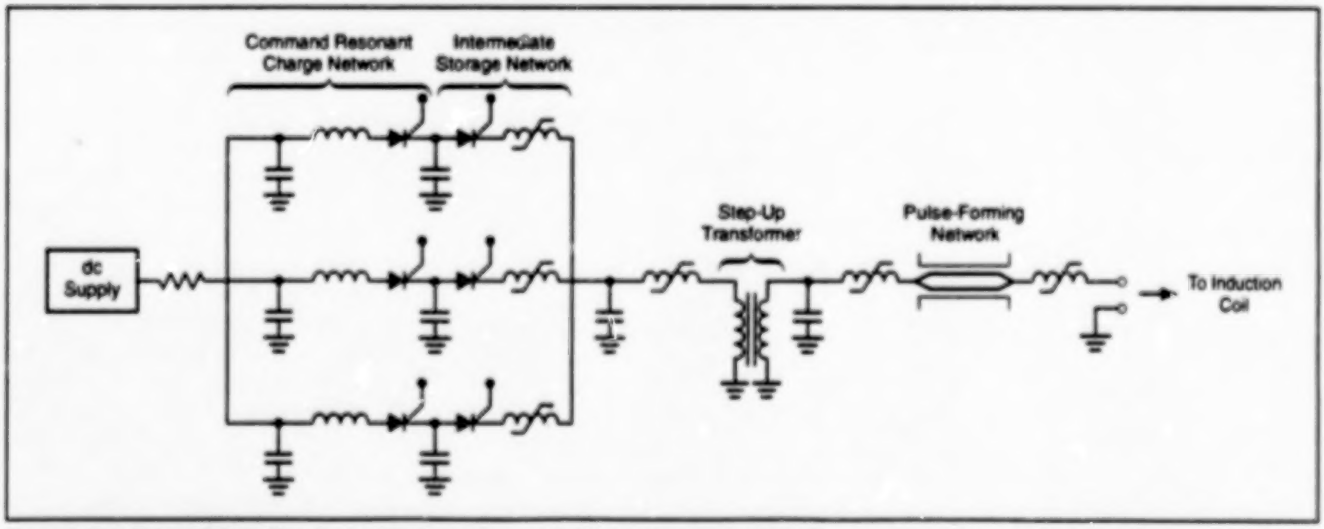


Figure 2. This **Pulsed Driver Circuit** converts dc input power to short, high-voltage pulses. For example, with a suitable choice of components, it can covert 500-Vdc input to 50-kV, submicrosecond pulses. A pulsed driver circuit for a specific application could differ in such details as the numbers, ratings, and placements of capacitors, inductors, and SCRs.

able, long-life, efficient pulse power circuits. The gas spark-gap switches used in older pulsed inductive plasma accelerators are unreliable and short-lived (a few million pulses maximum) because of erosion of spark-gap electrodes and contamination of gases. With regard to efficiency, two major issues arise:

- The pulse delivered by the power circuit in a typical older pulsed inductive plasma accelerator is not shaped to maximize energy efficiency. Before breakdown, the self-inductance of the coil limits the initial current rise; after breakdown the magnetic flux of the plasma current opposes that of the coil, so that the net inductance is reduced and the current rises rapidly. However, what is needed for efficient operation is a rapid initial current rise to obtain a strong electric field for uniform breakdown, followed by a slower current rise during acceleration to reduce resistive loss of energy in the plasma.
- Because of variation of the load impedance with acceleration of the plasma, some (typically 20 to 25 percent) of the energy fed to the accelerator is reflected. If the reflected energy can be recovered, then efficiency can be increased. The pulse-power circuits of older pulsed inductive plasma accelerators are not designed to recover the reflected energy.

In the developmental pulsed inductive plasma accelerators, the issues of optimal pulse shaping, recovery of reflected energy, and reliability of the switches are all addressed in the design of advanced pulsed driver circuits. These are compact, lightweight, modular solid-state circuits that contain (1) inductive and capacitive elements for storing energy and shaping pulses and (2) silicon controlled rectifiers (SCRs) for switching. Figure 2 shows a simplified version of a circuit of this type to illustrate the principle of operation. The input stage of the circuit is a command resonant charge (CRC) network controlled via SCRs. The CRC network delivers a preset quantity of charge and energy to intermediate storage capacitors between pulses. The pulses formed by the CRC are then compressed by a nonlinear inductance-and-capacitance network that includes a step-up transformer to obtain desired impedance levels.

The nonlinear circuit elements are inductors with saturable cores. The core of each following stage is allowed to saturate before a significant fraction of energy stored in the capacitors of the immediately preceding stage is transferred. The nonlinear saturation phenomenon increases the resonant frequency. Thus, energy is coupled progressively faster as it propagates through successive stages from the input to the output end. The circuit is efficient in transferring power in both directions because it not only upshifts frequency in the forward direction as described above but also downshifts frequency as a reflected pulse propagates back toward the input end. Energy reflected from a mismatched load can propagate all the way back to the SCR commutator. There, an energy-recovery circuit (omitted for clarity) that comprises inductors, capacitors, and SCRs stores some of the reflected energy, which is then added to the forward-propagating energy on the next pulse.

This work was done by Dennis A. Rally, Xing Chen, and William Guss of Science Research Laboratory, Inc., for **Lewis Research Center**. *Further information is contained in a TSP [see page 1].*

Inquiries concerning rights for the commercial use of this invention should be addressed to NASA Lewis Research Center, Commercial Technology Office, Attn: Tech Brief Patent Status, Mail Stop 7-3, 21000 Brookpark Road, Cleveland, Ohio 44135. Refer to LEW-16620.

Solar-Cell System With High Conversion Efficiency

Sunlight is spectrally dispersed to multiple cells, each responsive to part of the spectrum.

NASA's Jet Propulsion Laboratory, Pasadena, California

Cell Type	Spectral Region of Maximum Response	Measured Efficiency, Percent (1)	Percent Contribution to System Efficiency, Calculated for Optimized Optics
Ge	Near Infrared		9.17 (2)
Si	Red or Near Infrared	7.53	12.05
GaAs	Orange and Red	9.99	15.98
$GaInP_2$	Green and Yellow	5.57	8.91
GaN or GaP	Ultraviolet and Blue		2.73 (2)
Projected System Efficiency			48.84

Footnotes:
(1) At a concentration of 7 Suns measured at a prism lens.
(2) Estimated from the literature, without correction for concentration.

Each Type of Photovoltaic Cell responds maximally in a unique part of the spectrum, thereby contributing to overall efficiency in the conversion of spectrally dispersed sunlight to electricity.

A concept for obtaining high energy-conversion efficiency in a solar photovoltaic system involves (1) concentration and spectral dispersion of sunlight and (2) use of several types of solar photovoltaic cells, each placed at its optimum location in the spectrum. The spectral dispersion and concentration of sunlight can be effected by use of mirrors or lenses combined with prisms. The photovoltaic cells can be of the conventional single-junction type, which cost less than do the more advanced multijunction cells.

Preliminary experiments to demonstrate the feasibility of this concept were performed on several types of cells, using artificial sunlight and prisms that had not been optimized. On the basis of these experiments plus references to the literature, it has been estimated that an optimized system of this type could perform with an energy-conversion efficiency approaching 50 percent (see table). In contrast, the more-expensive multijunction solar cells yield efficiencies between 20 and 30 percent, while the efficiencies of conventional solar cells range from 11 to 19 percent in white light.

This work was done by Wayne Phillips of Caltech for **NASA's Jet Propulsion Laboratory**. *Further information is contained in a TSP [see page 1].*

NPO-20354

Packaging Electronic Circuits in Multi-Board Modules

Neither cables nor traditional connectors are used within modules.

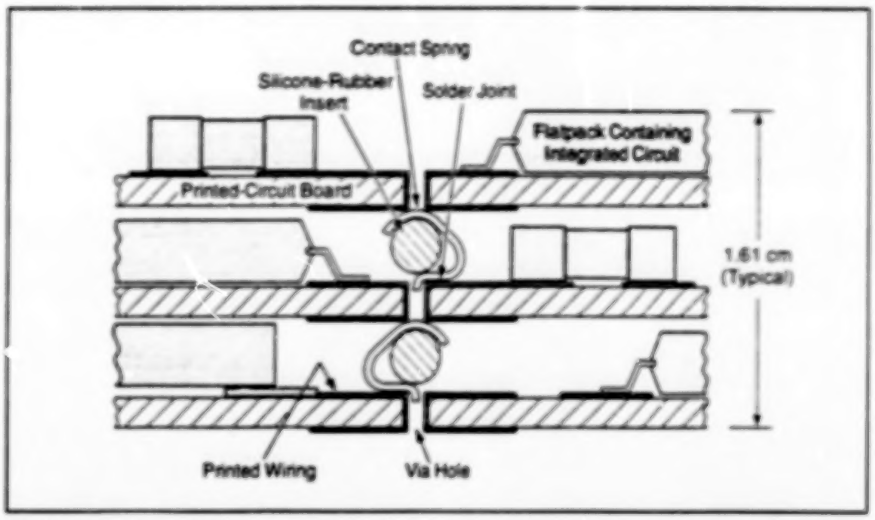
NASA's Jet Propulsion Laboratory, Pasadena, California

The Multi-Board Module (MBM) scheme has been conceived to provide a cost-effective way to combine digital electronic circuits into dense, lightweight packages, within which high-speed signals can be transmitted readily along three-dimensional conductive paths with minimal lengths. As the title suggests, the MBM scheme involves stacking of circuit boards in modules. Unlike in other circuit-packaging schemes, neither cables nor traditional electrical connectors are used to make the electrical connections among circuit boards in a module. Inasmuch as connectors and cables typically occupy a large fraction of the volume and constitute a large fraction of the mass of a package, the MBM scheme offers the potential for significant reductions in size and weight.

As shown in the figure, the connections between two adjacent circuit boards are made via gold-plated beryllium/copper contact springs. Each contact spring is soldered to printed wiring at a via hole on one of the boards. During assembly, each spring is pushed into contact with the printed wiring at a via hole at the corresponding location on the adjacent board. Inserts made of silicone rubber can be used to reinforce the contact springs.

In addition to eliminating the cost, weight, and bulk of cables and traditional electrical connectors, this contact scheme affords several advantages:

- The contacts are self-aligning and structurally reliable.
- Maintenance, repair, and testing are possible because circuit boards can readily be removed from stacks.
- To facilitate testing, one can turn off selected contacts by inserting insulating tabs; alternatively or in addition, one can insert thin conductive pads at selected contacts to gain access for probing.
- Unlike in conventional edge connection and in other three-dimensional-connection schemes, contacts can be located almost anywhere on the circuit boards; this makes it possible to reduce signal-path lengths and thereby accommodate higher-speed signals.



Contact Springs made of beryllium/copper provide electrical connections between printed-wiring traces on adjacent circuit boards stacked in a module.

In applying the MBM concept, designers might have to contend with limits on the sizes of modules and with guidelines regarding the numbers and placements of contacts and structural supports. High circuit densities could give rise to a need for thermal straps for additional heat sinking. Under some circumstances, it could be necessary to design against a tendency for contacts to open when the circuit boards are subjected to strong vibrations.

This work was done by John D. Baker and Alberto Montalvo of Caltech for **NASA's Jet Propulsion Laboratory**. *Further information is contained in a TSP [see page 1].*

In accordance with Public Law 96-517, the contractor has elected to retain title to this invention. Inquiries concerning rights for its commercial use should be addressed to

Technology Reporting Office
JPL
Mail Stop 122-116
4800 Oak Grove Drive
Pasadena, CA 91109
(818) 354-2240

Refer to NPO-19972, volume and number of this NASA Tech Briefs *issue, and the page number.*

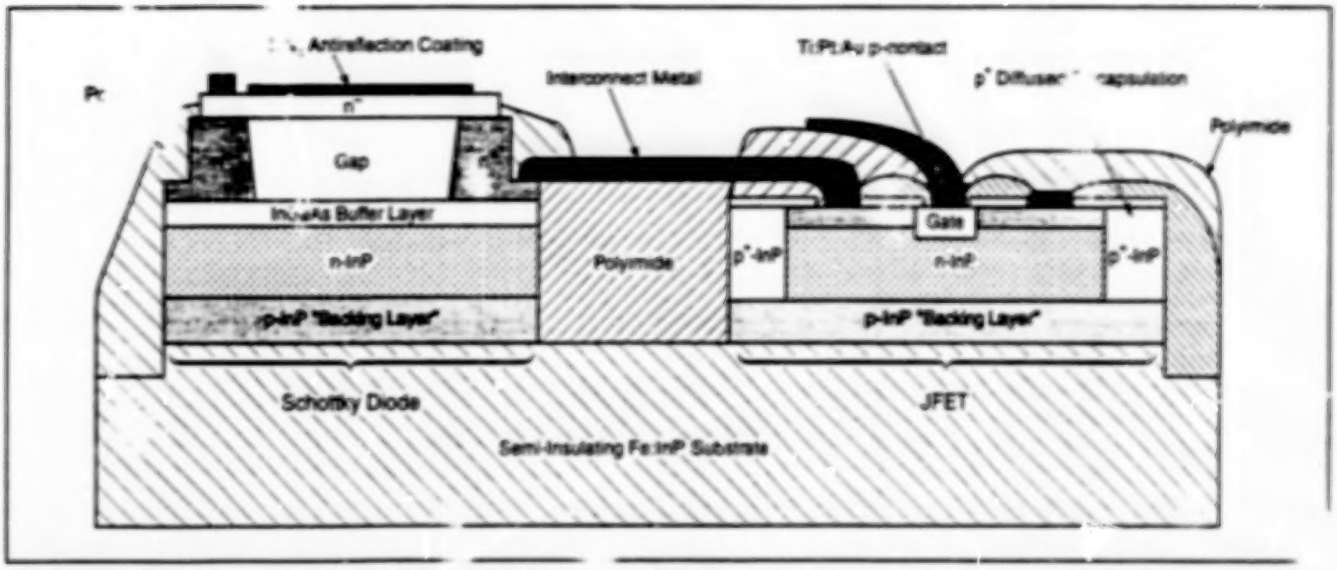
Dual-Function Microelectronic Sensors

Scenes could be imaged a visible/infrared band, an infrared band, or both.

NASA's Jet Propulsion Laboratory, Pasadena, California

Integrated-circuit image sensors of a proposed type would be capable of operation in either the wavelength band of 0.5 to 2.5 μm, the wavelength band of 2.8 to 5.8 μm, or both bands simultaneously. Called "dual function, thermal optical image sensors" (DTOISs), these sensors could be useful in a variety of scientific, industrial, and medical applications in which there are needs for visible and infrared imaging — typically, for noncontact measurements of temperature distributions. In medicine, for example, such measurements could provide early indications of developing tumors.

Each pixel of a DTOIS (see figure) would contain a "lifted," bridged InGaAs Schottky diode for sensitivity in the 2.8-to-5.8-μm band, integrated with an InP junction field-effect transistor (JFET). Also integrated with the bridged Schottky diode and JFET would be the already developed InGaAs positive/intrinsic/negative (PIN) photodiode (not shown in figure) for sensitivity in the 0.5-to-2.5-μm band. Each of these sensory devices would be connected to a dedicated active pixel readout circuit so that the image in either or both wavelength band(s) could be read out. The pixel-addressing scheme of the readout circuits would involve the use of JFETs instead of conventional multiplexers.



The **Sensory Devices** in each pixel of a DTOIS would be a lifted Schottky diode (sensitive in the longer-wavelength infrared band) and a PIN diode (sensitive in the shorter-wavelength visible/infrared bands, not shown in the figure) with JFET(s).

The planned development of the DTOISs would build on previous accomplishments in the continuing development of InGaAs active-pixel sensor arrays, each pixel of which contains an InGaAs photogate-type sensory device integrated with a low-leakage InP JFET. The planned development would also incorporate techniques developed previously for the fabrication of GaAs Schottky diodes for operation at frequencies from 240 to 640 GHz. Current plans for proof of the DTOIS concept call for development of a prototype DTOIS for a microbiological application. The major technical challenge will be to design a lifted Schottky diode to increase thermal sensitivity so that spatial, temporal, and thermal resolutions could be superior to those of pre-existing detectors. Inasmuch as an array of lifted Schottky diodes would supplant the silicon-resistor arrays of state-of-the-art thermal sensors, the thermal resolution of the DTOIS is expected to be finer than the value of 0.04 K claimed previously for a monolithic silicon focal-plane array. Also, because of the high charge-carrier mobility of InGaAs, the thermal response of the DTOIS is expected to be faster than that of a silicon sensor by a factor of about 6. The ability to detect photons in the 2.8-to-5.8-μm wavelength band would constitute an additional advantage over a silicon sensor.

This work was done by Quiesup Kim of Caltech for **NASA's Jet Propulsion Laboratory**. *Further information is contained in a TSP [see page 1].*

In accordance with Public Law 96-517, the contractor has elected to retain title to this invention. Inquiries concerning rights for its commercial use should be addressed to

Technology Reporting Office
JPL
Mail Stop 122-116
4800 Oak Grove Drive
Pasadena, CA 91109
(818) 354-2240

Refer to NPO-20430, volume and number of this NASA Tech Briefs *issue, and the page number.*

Luneberg Lenses Made of Open-Cell Polyurethane Foams

Advantages would include light weight and ease of fabrication.

NASA's Jet Propulsion Laboratory, Pasadena, California

A Luneberg lens is a microwave lens consisting of a series of concentric shells of differing dielectric constants. The highest dielectric constant, or refractive index, resides at the core and the lowest, at the outer shell. Microwaves passing through this arrangement of shells are focused in the same manner as light passing through a glass lens.

Known for decades, Luneberg lenses have been fabricated from materials such as polystyrene foam, foamed glass, and other cellular materials. The dielectric constant is controlled by simply controlling the bulk density of the foam. Materials, such as foamed polystyrene, are useful for ground-based applications, but space deployment imposes severe restrictions on their use. The closed-cell materials used in the past are frequently difficult to fabricate and are high in mass and tend to exhibit electrical and dimensional instabilities. They may also be expensive and vulnerable to fracture by ground handling or launch vibrations.

This concept proposes Luneberg lenses suitable for space applications and fabricated from open-celled elastomeric foams. An ideal candidate is the class of foamed urethane polymers. The dielectric constant of these materials is controlled by varying the density of the foam, but may also be varied by addition of polar groups (e.g., ethoxy, sulfonyl, carboxylate, trifluoropropoxy, and the like) to the polymer backbone. Unlike increasing the dielectric constant by the addition of conductive compounds, this approach maintains the electrons in the valence band and consequently keeps the loss tangent low.

Urethane is the most widely used chemistry in the fabrication of open-celled foam materials, with densities ranging from 1.2 to 10 lb/ft^3 (19.2 to 160 kg/m^3). Dielectric constants typically vary from 1.05 to 4.0 at high densities, and loss tangents vary from immeasurably small to 5 ×

10^{-3}. Both mechanical and dielectric properties are identical in all axes (isotropic), solving a significant problem with previous materials choices. These open-celled foams are inexpensive, easy to machine, and low in density. Their open cell structure results in rapid and complete air release in the vacuum of space. The inherent resilience of these materials gives them high mechanical damping, resistance to fracture during handling and launch, and additionally provides a positive restoring force to their dimensions. This "self-correcting" property overcomes the "airgap" problem of previous designs, in which a slight separation between the shells results in an internal reflection and loss of RF (radio-frequency) efficiency. Finally, these materials have extremely low thermal conductivity (typically 0.05 W/m-K). This last characteristic prevents the lens structure from undergoing dramatic temperature swings in response to a changing thermal environment, and further improves their electrical stability. Luneberg lenses fabricated from these inexpensive open-celled urethane foams may additionally be supported for use by a thin-walled lightweight shell of some other material, such as fiber glass.

This work was done by Paul B. Willis of Caltech for **NASA's Jet Propulsion Laboratory**. *Further information is contained in a TSP [see page 1].*

In accordance with Public Law 96-517, the contractor has elected to retain title to this invention. Inquiries concerning rights for its commercial use should be addressed to

Technology Reporting Office
JPL
Mail Stop 122-116
4800 Oak Grove Drive
Pasadena, CA 91109
(818) 354-2240

Refer to NPO-20339, volume and number of this NASA Tech Briefs issue, and the page number.

BLANK PAGE



Electronic Systems

Hardware, Techniques, and Processes

15 Frequency-Agile Fiber-Optic Transceivers

BLANK PAGE

Frequency-Agile Fiber-Optic Transceivers

These transceivers handle data signals over a 30:1 frequency range.

Goddard Space Flight Center, Greenbelt, Maryland

Fiber-optic transceivers (FOTs) that can handle digital signals at any bit rate from 10 to 300 MHz have been developed. These variable-rate FOTs offer considerable advantages over fixed-rate FOTs that have been used until now. A fixed-rate FOT contains clock- and data-signal-recovery circuits tuned to the data rate. In a system in which data streams are transmitted at different rates, the data rates must be specified in advance, and a separate fixed-rate FOT must be designed, constructed, and installed for each rate. Thus the cost of acquiring, maintaining, and operating fixed-rate FOTs for a multiple-rate system can be high, and under some circumstances, advance notice of data rates could compromise security. Obviously, costs can be reduced and security enhanced by use of variable-rate FOTs capable of operating over the full range of data rates.

Each transceiver includes a transmitter and a receiver module (see figure). The primary function of the transmitter module is performed in an encoder, which inserts one overhead bit for every eight data bits in a non-return-to-zero (NRZ) serial data stream. The overhead bits are used to prevent lockup in a scrambler, and they remove all constraints on the input data pattern. The rate of the transmitted serial data stream is thus 9/8× the input data rate.

In the receiver module, an optical receiver converts the incoming light signal to a bit-serial electrical signal. This electrical signal is fed to a clock-signal-recovery circuit, which implements a method, called "variable bit synchronization" (VBS), for recovering a clock signal characterized by a rate that could vary over a wide range. In VBS, the synchronous clock signal is reconstructed from the composite (clock + data) bit-serial electrical signal, then the data signal is regenerated with reclocking. The VBS process is what makes it possible to transmit NRZ data and clock signals over a communication channel and to recover these signals within a wide frequency range.

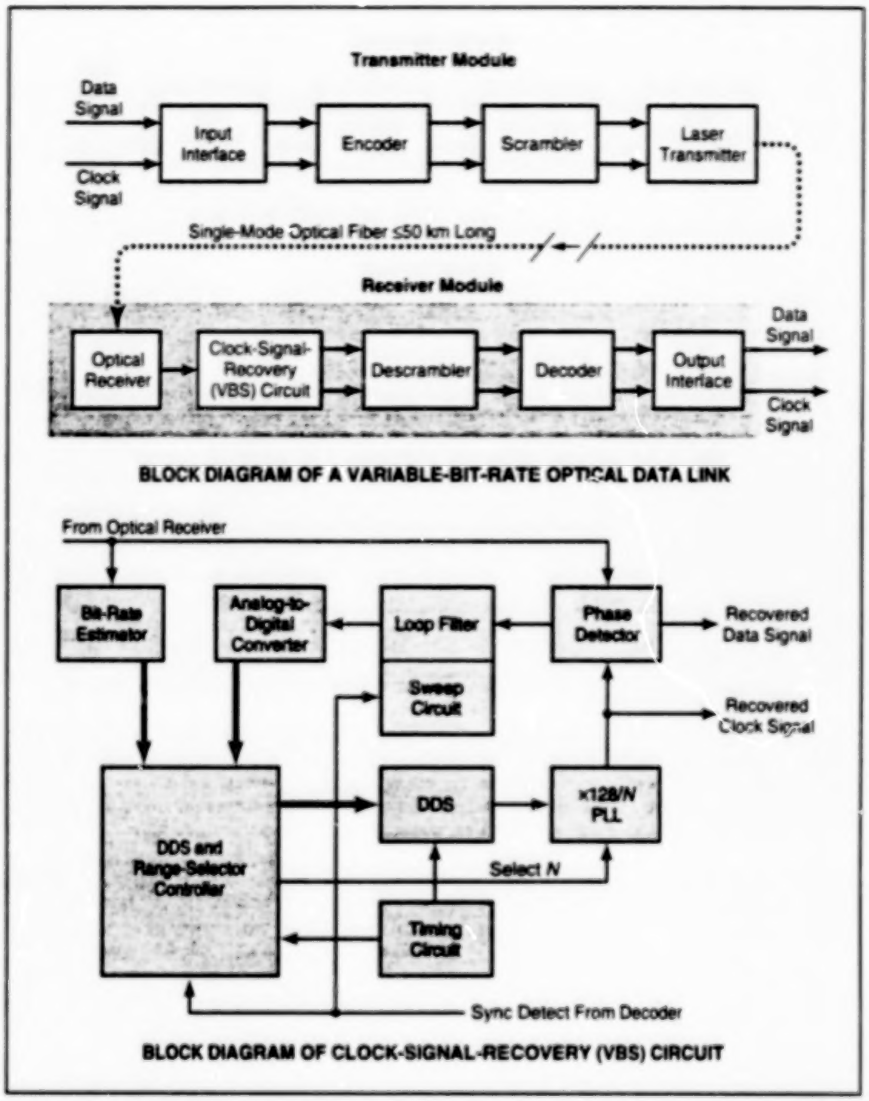
The lower part of the figure illustrates the clock-signal-recovery circuit and the VBS process in more detail. A bit-rate estimator provides an estimate of the incoming data rate. The estimate is used by a direct digital synthesizer (DDS) to acquire the clock frequency and achieve synchronization as follows: The output of the DDS is processed through a phase-lock loop that multiplies frequency by a factor of 128/*N* (where *N* is an integer). A controller sets up the DDS and PLL to generate a signal with a frequency within 3 percent of the actual clock frequency. The DDS is then swept into exact frequency and phase lock by a vernier sweep circuit. Typically, the clock-signal-acquisition process takes about 2 seconds.

The clock and data outputs of the clock-signal-recovery circuit are fed to a descrambler. The output of the descrambler is fed to a decoder, which strips off and frame-locks to the overhead bits and reconstructs the original NRZ data stream. The decoder also performs an 8/9 frequency multiplication on the reconstructed clock signal to recover the clock signal of the original data stream. The overhead bits and the frame-synchronization process that involves the overhead bits provide a benefit of continuous in-service error detection.

One particularly attractive feature of the variable-rate FOT is its ability to function without intervention by a technician once it has been installed. In operation, the receiver reconstructs the original clock and data signals at their original rates, with a bit-error rate of 10^{-12} or less.

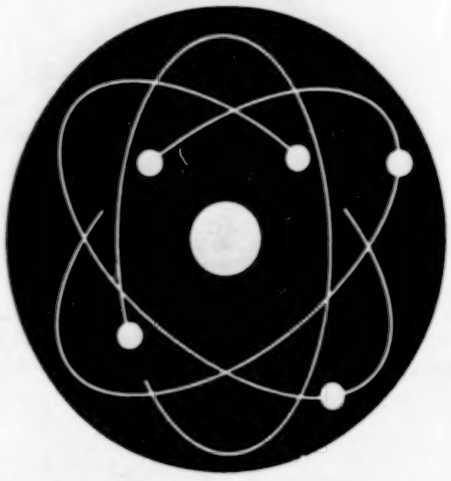
This work was done by Chi Le of **Goddard Space Flight Center**, *Paul Casper of Broadband Communications Products, and Jim Shaughnessy of Computer Sciences Corp. Further information is contained in a TSP [see page 1].*

GSC-13782



The Clock-Signal-Recovery Circuit Is the Critical Unit that implements the VBS process and thereby enables the fiber-optic transceiver to handle data at any rate over a wide range.

BLANK PAGE



Physical Sciences

Hardware, Techniques, and Processes

19 Thermal-Isolation Structure for Low-Temperature Experiments
19 Apparatus for Faster Ultrasonic-Lamb-Wave Testing
20 Reactive-Insulator SiC-Based Schottky Diodes as Gas Sensors
22 Fabry-Perot Fiber-Optic Temperature Sensor
23 Optical Cavity-Ring-Down Measurement of Soot Concentration
24 Integrated Electrochemical Sulfur Dioxide Sensors
25 In Situ Chemical Analysis via Acoustic-Emission Spectra
25 Electrostrictive Thermal Break Between Superfluid Reservoirs

Books and Reports

26 Experiments on Flow in a Model Compressor Drum

BLANK PAGE

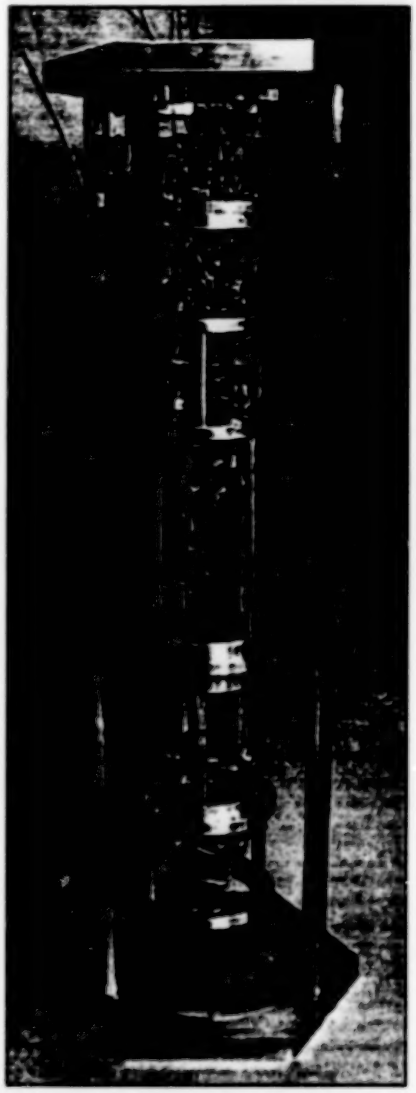
Thermal-Isolation Structure for Low-Temperature Experiments

A tension/compression structure reduces thermal bias.

NASA's Jet Propulsion Laboratory, Pasadena, California

The figure shows a tension/compression structure that provides rigid suspension and a high degree of thermal isolation for a small instrument assembly used in low-temperature experiments. The structure is designed primarily for use in a microgravitational environment; specifically, to support a sensor package in the Critical Dynamics in Microgravity Experiment (DYNAMX), which is scheduled to fly on the space shuttle as part of the Microgravity Science Payload in early 2002. The structure also is adaptable to scientific experimentation in normal Earth gravity in cases in which there are requirements for lightweight, rigid, thermally isolating structures in confining geometries.

High structural rigidity is necessary for low-temperature scientific experimentation in the microgravitational environment of a spacecraft in a low orbit around the Earth. The rigidity is needed not only to withstand loads encountered during launch but also to prevent amplification of low-frequency vibrations from the spacecraft (typically, the space shuttle), which vibrations can generate heat in an instrument and thereby bias the results of an experiment. High levels of thermal isolation are needed, not only between the instrument and the spacecraft, but also between components within the instrument, to prevent thermal "crosstalk" and the biases that such crosstalk could engender. In the case of a highly sensitive low-temperature instrument, the need for thermal isolation dictates minimization of instrument-component masses to minimize the bias attributable to heat deposited by cosmic rays.



In this Tension/Compression Structure polymeric cords under tensile preload provide rigid suspension and thermal isolation of the suspended mass.

Heretofore, tension/compression structures have seldom been used in cryogenic applications, even though they offer enormous advantages in thermal isolation and rigidity. The present tension/compression structure includes a cylindrical exoskeleton, within which instrument components are held in position by tensioned Kevlar (or equivalent) aromatic polyamid cords. The combination of strength of the exoskeleton and preload in the cords provides rigid mounting for the instrument components. Because the cross-sectional area of the cords is small and the thermal conductivity of the cord material is low, the cords provide a high level of thermal isolation. The narrowness and low density of the cords also limits the deposition of heat from cosmic rays.

A computational simulation was performed to compare the performance of this structure with the performances of mounting structures of conventional designs. The results of the simulation showed that this structure could provide a higher level of thermal isolation from surrounding structures and a lower level of thermal crosstalk between instrument components.

This work was done by Alfred Nash and Linda Robeck of Caltech for **NASA's Jet Propulsion Laboratory**. *Further information is contained in a TSP [see page 1].*

NPO-20338

Apparatus for Faster Ultrasonic-Lamb-Wave Testing

Data on the stiffness properties of a specimen can be acquired within seconds.

NASA's Jet Propulsion Laboratory, Pasadena, California

An ultrasonic-transducer fixture containing multiple pairs of fixed transducers, plus associated electronic transducer-multiplexing circuitry have been developed to accelerate the acquisition of data on the dispersion of ultrasonic leaky Lamb waves (LLWs) in plate specimens of laminated composite (matrix/fiber) materials. The fixture and multiplexing circuitry can readily be incorporated into a previously constructed ultrasonic-LLW system that contains a single pair of movable ultrasonic transducers.

LLWs are guided waves that propagate along the surfaces of the specimens. In a typical conventional ultrasonic-LLW system, a plate specimen is immersed in water (which serves as an acoustic-coupling medium), with a transmitting and a receiving ultrasonic transducer positioned above the specimen in a pitch/catch arrangement at a specified angle of incidence, as shown in Figure 1. For each of several angles of incidence, the output of the receiving transducer is digitized and processed to extract reflection-spectrum and dispersion data. These data are then inverted, by use of special-purpose software, to obtain the coefficients of elasticity of the materials and to evaluate flaws in the specimens.

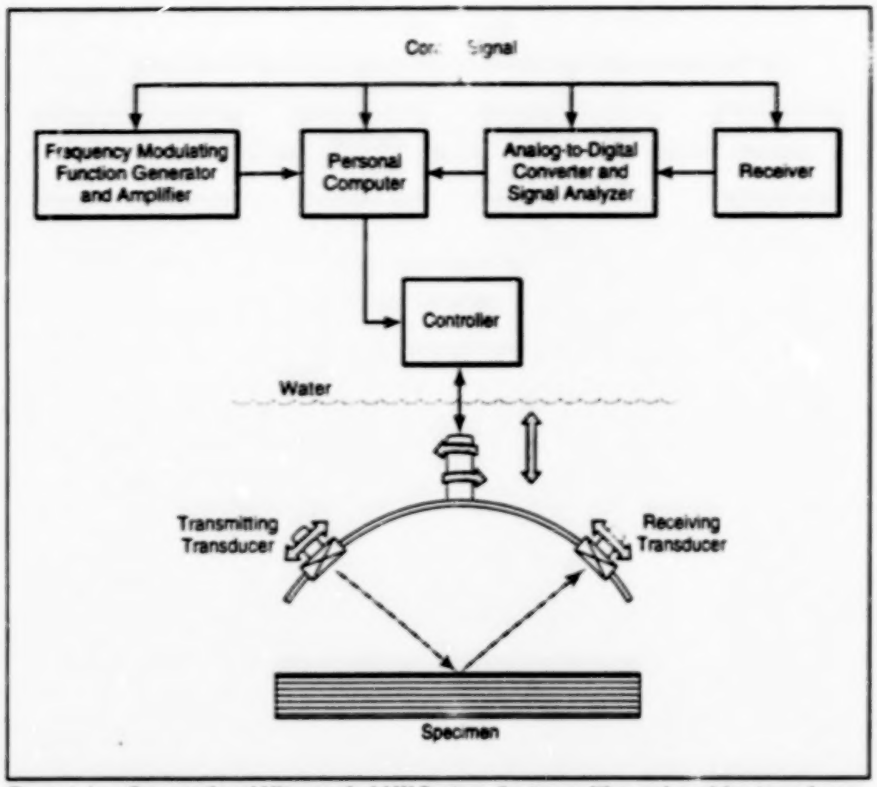


Figure 1. In a **Conventional Ultrasonic-LLW System**, the transmitting and receiving transducers must be moved to different positions to obtain different angles of incidence.



Figure 2. **Transmitting/Receiving Pairs of Ultrasonic Transducers** in this fixture are positioned and oriented, relative to an immersed specimen, for angles of incidence of 15°, 30°, 45°, and 60°.

In the conventional system, the speed of acquisition of data is limited by the need to reposition the transducers to obtain different angles of incidence. In a system equipped with the present fixture and multiplexing circuitry, data can be acquired much more rapidly because except as explained in the next paragraph, the transducers are not repositioned during a test; instead, multiple transmitting/receiving pairs of transducers are pre-positioned at the desired angles of incidence (see Figure 2) and are switched into and out of operation in the required sequence during a test by use of the multiplexer circuits under control by a computer. The software for controlling the multiplexer circuits is part of a modified version of the software for controlling the rest of the ultrasonic-LLW system.

In some cases, it could be necessary to acquire data with the plane of incidence at different polar angles (0°, 45°, and 90°) with respect to fibers projected onto the surfaces of the specimens in order to characterize the specimen materials completely. Even in such a case, it is not necessary to expend much time repositioning transducer pairs; all one need do is rotate the transducer fixture to each polar angle and to perform the measurement sequence there. Experiments have shown that dispersion data for four angles of incidence at one given polar-angle setting could be acquired in 7.4 seconds.

This work was done by Yoseph Bar-Cohen of Caltech and Susan Kersey, Cedric Daksla, and Anatoly Blanovsky of UCLA for **NASA's Jet Propulsion Laboratory**. *Further information is contained in a TSP [see page 1].*

In accordance with Public Law 96-517, the contractor has elected to retain title to this invention. Inquiries concerning rights for its commercial use should be addressed to

Technology Reporting Office
JPL
Mail Stop 122-116
4800 Oak Grove Drive
Pasadena, CA 91109
(818) 354-2240

Refer to NPO-20400, volume and number of this NASA Tech Briefs *issue, and the page number.*

Reactive-Insulator SiC-Based Schottky Diodes as Gas Sensors

High-temperature gas sensors are being developed.

Lewis Research Center, Cleveland, Ohio

Improved silicon carbide-based Schottky diodes are undergoing development for use in detecting hydrocarbon (C_xH_y) and nitrogen oxide (NO_x) gases at high temperatures. In comparison with gas sensors of other types, Schottky-diode gas sensors exhibit relatively high sensitivity — an advantage for monitoring engine-exhaust emissions and hazardous gases emitted in low concentrations. SiC-based Schottky diodes can function at temperatures too high for Si-based devices; beyond the

obvious advantage of a wider operating-temperature range, this opens the possibility of incorporating into sensors materials that react with C_xH_y and NO_x at high temperatures in ways that enhance sensitivity, selectivity, and/or stability.

The simplest Schottky-diode gas sensor is a metal/semiconductor (MS) device; it includes an electrode made of a catalytic metal (in this case, Pd) deposited on a semiconductor (in this case, SiC). For hydrogen and hydrocarbons, the gas dissociates on the exposed surface of the metal and diffuses to the metal/semiconductor or metal/insulator interface, forming a dipole layer that changes the electronic properties of the Schottky diode in proportion to the amount of the gas.

The SiC-based Schottky-diode gas sensors that are the subjects of the present development efforts are metal/reactive-insulator/semiconductor (MRIS) devices. In contrast to standard metal/insulator/semiconductor (MIS) structures, the insulators in a MRIS structure are chosen for their reactivity to the gas of interest. In the fabrication of an MRIS device, an electrically insulating layer of metal oxide (for example, SnO_2) is incorporated between the catalytic electrode and the SiC semiconductor layer to obtain the advantageous high-temperature characteristics mentioned above. More specifically:

- Sensitivity is increased because the C_xH_y or NO_x gas reacts with the reactive oxide insulating layer as well as with the catalytic metal;
- The sensor can be made more stable in that the oxide layer can act as a barrier between the metal and the SiC; and
- The selectivity of the sensor can be varied by varying the oxide layer.

In preparation for comparative experiments, both Pd/SiC and Pd/SnO_2/SiC Schottky diodes were fabricated on the same chip. The two diodes were the same except that Pd/SnO_2/SiC diodes included sputter-deposited layers of SnO_2 about 50 Å thick.

The current-vs.-voltage responses of these diodes were measured during exposures to air and to a mixture of 400 parts per million (ppm) H_2 in N_2, at a temperature of 350 °C. The results of these measurements (see Figure 1) on the Pd/SnO_2/SiC diode show parallel shunt resistance at potentials below 1.0 V; proceeding upward from 1.0 V, the data show exponential Schottky behavior at first, with series resistance increasing and beginning to dominate at the high end of the voltage range. Analysis of the exponential portion of the curve leads to the conclusion that the SnO_2 layer increased the Schottky barrier height.

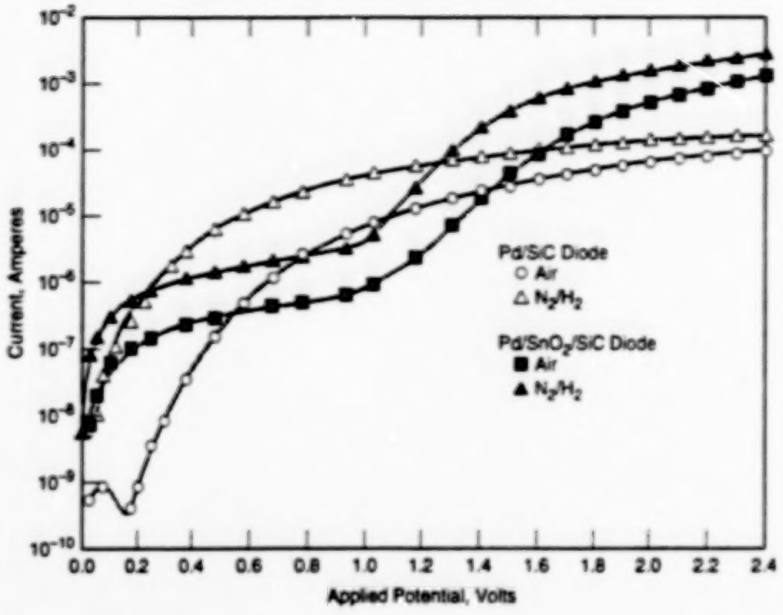


Figure 1. These Current-vs.-Voltage Measurements of Pd/SiC and Pd/SnO_2/SiC gas-sensing diodes show how the SnO_2 layer alters the electrical characteristics and the response to H_2 gas.

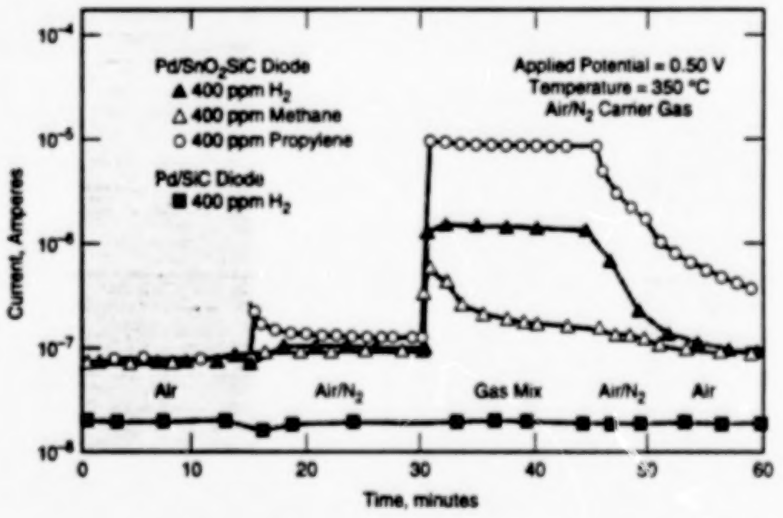


Figure 2. These Current Responses at Constant Voltage measured on thermally aged Pd/SiC and Pd/SnO_2/SiC diodes show that the SnO_2 layer had prevented or at least reduced the degradation effected by the aging process.

The effect of the 400 ppm H_2 in N_2 was to increase the current at a given voltage. One of the effects of the SnO_2 layer was to impart higher sensitivity to H_2 in the Schottky-like conduction region. The Pd/SiC diode behaved differently, exhibiting an exponential response in the low-voltage region and series-resistance effect at higher voltages. These results clearly show that the SnO_2 layer changed the basic electronic behavior and the response to H_2.

The stability and sensitivity of the sensors were also improved using the MRIS structure. Pd/SiC and Pd/SnO_2/SiC diodes were aged for several weeks at a temperature of 350 °C. In the experiments, these diodes were exposed, variously, to H_2, methane, or propylene at a concentration of 400 ppm in a carrier gas mixture of N_2 and air, at a temperature of 350 °C. During these exposures, diode currents were measured as a function of time at a fixed applied potential of 0.5 V. The results (see Figure 2) indicate that the Pd/SiC diode had been degraded during the aging process, in that this diode did not respond to H_2 in the air/N_2 carrier gas at the end of the experiment. It also did not respond to propylene

or methane (not plotted in the figure). In contrast, the Pd/SnO_2/SiC diode responded to hydrogen, methane, and propylene. Thus, the SnO_2 layer made it possible to detect gases that would otherwise not be detected and enabled the desired longer-term operation of the sensor. Variation of the type of reactive insulator is expected to produce different gas sensitivities.

This work was done by Gary W. Hunter and Philip G. Neudeck of **Lewis Research Center**, *Dak Knight of Cortez III, Chung-Chiun Liu and Quing-Hai Wu of Case Western Reserve University, and Liang-Yu Chen of National Research Council. Further information is contained in a TSP [see page 1].*

Inquiries concerning rights for the commercial use of this invention should be addressed to NASA Lewis Research Center, Commercial Technology Office, Attn: Tech Brief Patent Status, Mail Stop 7–3, 21000 Brookpark Road, Cleveland, Ohio 44135. Refer to LEW-16544.

Fabry-Perot Fiber-Optic Temperature Sensor

This is a prototype of rugged sensors for use in advanced engines.

Lewis Research Center, Cleveland, Ohio

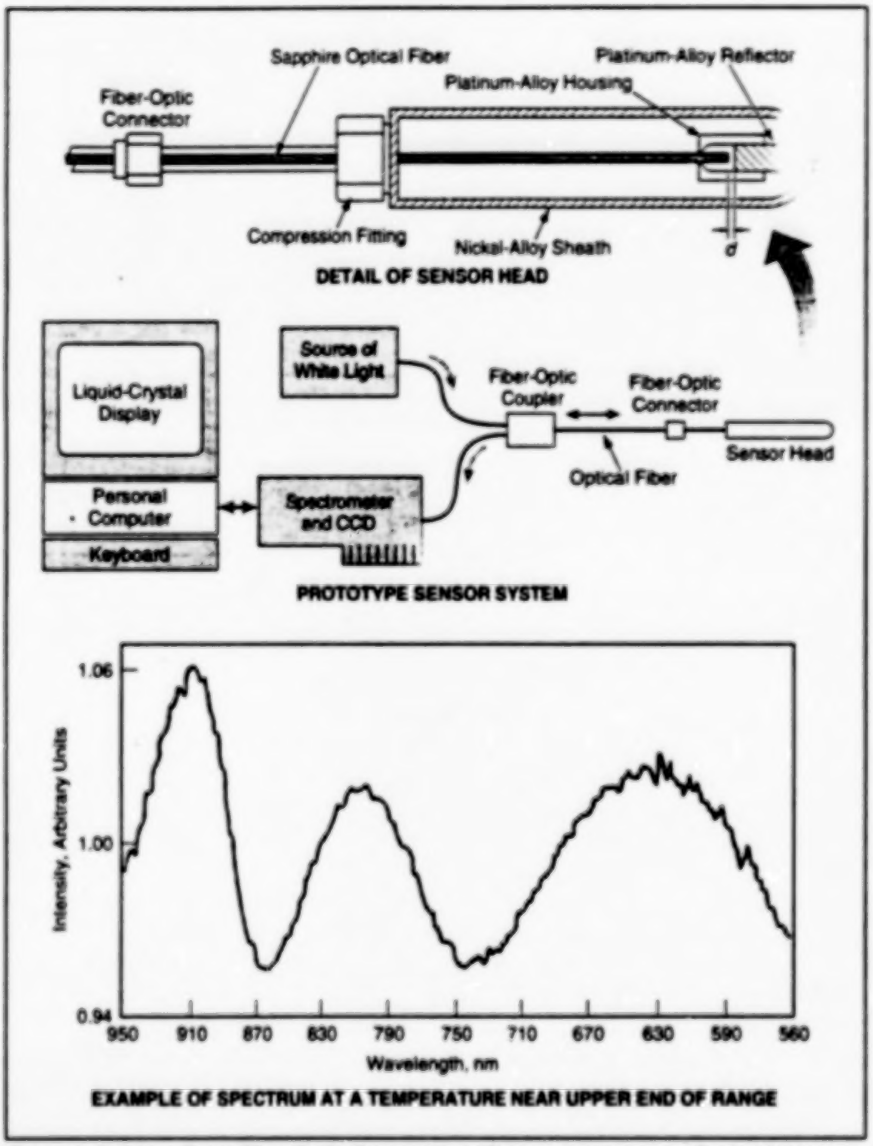


Figure 1. A Fabry-Perot Fiber-Optic Temperature-Sensor generates a reflected-light spectrum characteristic of the temperature in the sensor head.

A class of developmental photonic temperature-measuring systems is based on the use of miniature, fiber-optic-coupled Fabry-Perot interferometers as temperature transducers. These systems are intended for monitoring and control of advanced aircraft engines, conventional and nuclear powerplants, industrial plants, and other systems in which conditions could be too severe for electronic temperature sensors (thermocouples, thermistors, and bimetallic devices). Unlike electronic temperature sensors, these and other photonic temperature sensors do not pose a sparking hazard and are insensitive to electromagnetic interference at suboptical frequencies.

In essence, a Fabry-Perot fiber-optic temperature sensor provides a temperature-sensitive reflectance spectrum. Figure 1 illustrates a prototype Fabry-Perot fiber-optic temperature-sensor system that has been built and tested to demonstrate the feasibility of such systems for monitoring aircraft-engine exhaust temperatures from −50 to +600 °C. The sensor head comprises an Inconel™ (a nickel-alloy) sheath that contains the Fabry-Perot interferometer, which is located at the tip of a sapphire optical fiber that connects the sensor head to external instrumentation. A small platinum-alloy housing holds a reflector (made of the same alloy) at a short distance, *d*, from the fiber-optic tip, which is polished. The gap *d* defines the interferometer cavity.

White light is launched into the optical fiber via a 2:1 fiber-optic coupler at the end opposite the sensor head. The light travels along the fiber to the sensor head. About 4 percent of the incident light is reflected back along the fiber from the polished tip. The remainder of the incident light travels on to the platinum-alloy reflector, and about 90 percent of the light incident on the reflector re-enters the fiber and propagates back along the fiber, along with the light reflected from the fiber tip.

The fiber-optic coupler directs the two backward-propagating light beams to a spectrometer that is integrated with a 1,000-pixel linear charge-coupled-device (CCD) photodetector array on a computer plug-in spectrometer card. Because of interference between the two backward-propagating beams, the CCD output shows characteristic interference fringes; that is, a reflected-intensity-vs.-wavelength spectrum. Because of the difference between the coefficients of thermal expansion of the sapphire optical fiber and platinum-alloy housing and reflector, *d* varies with temperature, giving rise to a change in the spectrum. Among other things, the

number of interference fringes in this spectrum increases with temperature.

The raw reflectance spectrum is divided by the spectrum of the incident white light to obtain a normalized spectrum. The computer calculates the squared difference between the normalized spectrum and each of 117 stored calibration curves, which are normalized spectra that correspond to known temperatures at 5 °C increments. A parabolic interpolation is used for temperatures between the increments. The measured temperature is taken to be the temperature that yields the minimum squared difference.

In an experiment, the prototype Fabry-Perot fiber-optic temperature-sensor system was used, along with a thermocouple, to monitor the exhaust temperature of an aircraft engine. The Fabry-Perot temperature readings agreed closely with the thermocouple readings (see Figure 2). In more than 50 hours of flight tests, the prototype system proved to be immune to source fluctuations and to deterioration of optical surfaces inside the sensor head. The prototype system functioned under normal flight conditions and during severe maneuvers with accelerations as large as 4 times the normal Earth gravitational acceleration.

This work was done by Takeo Sawatari, Yuping Lin, and Phil Gaubis of Sentec Corp. for **Lewis Research Center**. *Sensor calibration and flight tests were conducted by Margaret L. Turne of* **Lewis Research Center** *and of Kristie A. Elam of Gilcrest Electric Co. Further information is contained in a TSP [see page 1].*

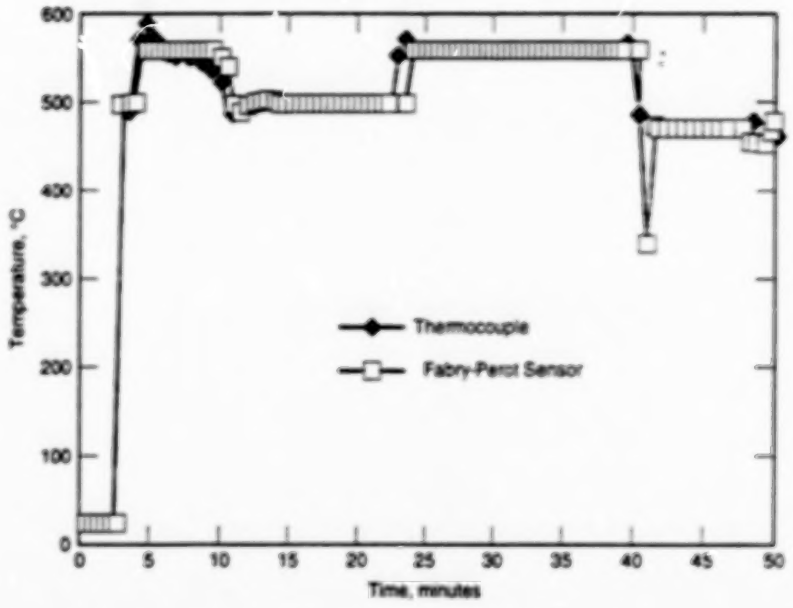


Figure 2. The Temperatures in These Plots were calculated from measurements taken during straight and level flight. The two sets of temperatures from measurements taken during severe maneuvers agreed almost as well.

In accordance with Public Law 96-517, the contractor has elected to retain title to this invention. Inquiries concerning rights for its commercial use should be addressed to

Takeo Sawatari
Sentec Corporation
2000 Oakley Park Road, Suite 205
Walled Lake, MI 48390

Refer to LEW-16610, volume and number of this NASA Tech Briefs *issue, and the page number.*

Optical Cavity-Ring-Down Measurement of Soot Concentration

Sensitivity and temporal resolution exceed those of any other technique now in use.

Lewis Research Center, Cleveland, Ohio

An optical technique for measuring the concentration of soot in air is based on the cavity-ring-down (CRD) principle, which is so named because it involves observation of the decay ("ring-down") of a signal echoing in a cavity. By use of (1) the observed rate of decay and (2) a known relationship between the rate of decay and the quantity of something that contributes to the decay, one calculates this quantity. In this case, the ring-down cavity is an optical one, the absorption and scattering of light by soot contributes to the decay of an optical signal, and the concentration of soot is the quantity to be determined from the measured rate of decay.

The ring-down cavity is bounded by two confocal mirrors with a radius of curvature equal to or greater than the distance between them. Pulsed laser light is prepared for coupling into the cavity by spatial filtering followed by down-collimation to match the TEM_{00} mode of the cavity. A photomultiplier tube or an amplified positive/intrinsic/negative (PIN) silicon photodiode detects light coming out of the cavity. The output of the photodetector is sent to a transient-signal digitizer. The digitized signal is processed to determine the ring-down time (τ) or, equivalently, its rate of decay (k).

The ring-down time is given by

$$\tau = \frac{1}{k} = \frac{d}{c\left[1 - R + \left(k_e f_v L/\lambda\right)\right]}$$

where d is the distance between mirrors, c is the speed of light, R is the reflectivity of the mirrors, k_e is a constant of proportionality for the amount of absorption of light in soot, f_v is the soot concentration (expressed as a volume fraction), L is the distance over which soot is distributed, and λ is the wavelength of the laser light. One potential source of error is uncertainty in the value of k_e; this value can be calculated from the index of refraction of soot, which is not known to better than about 10 percent. The equation can be solved for the concentration of soot:

$$f_v = \left(\lambda/k_e L\right)\left[\left(d/c\tau\right) + R - 1\right]$$

The sensitivity of this CRD technique exceeds that of any other soot-measurement technique now in use; it enables measurement of soot concentrations in the range from 1 to 100 parts per billion. The temporal resolution of this technique is also greater than that of any other soot-measurement technique. CRD has a good spatial resolution in directions orthogonal to the cavity axis but suffers from a lack thereof along this axis. However, CRD could be used along with laser-induced incandescence (LII), which gives spatially-resolved relative concentrations. Because the CRD

signal for a given path is proportional to the path-integrated LII signal. 2D measurements could be used to calibrate LII measurements. CRD, either alone or in combination with LII, could be used to measure concentrations of particulate matter in the atmosphere at large, in industrial plumes and in the exhausts of gasoline engines, diesel engines, power plants, and incinerators.

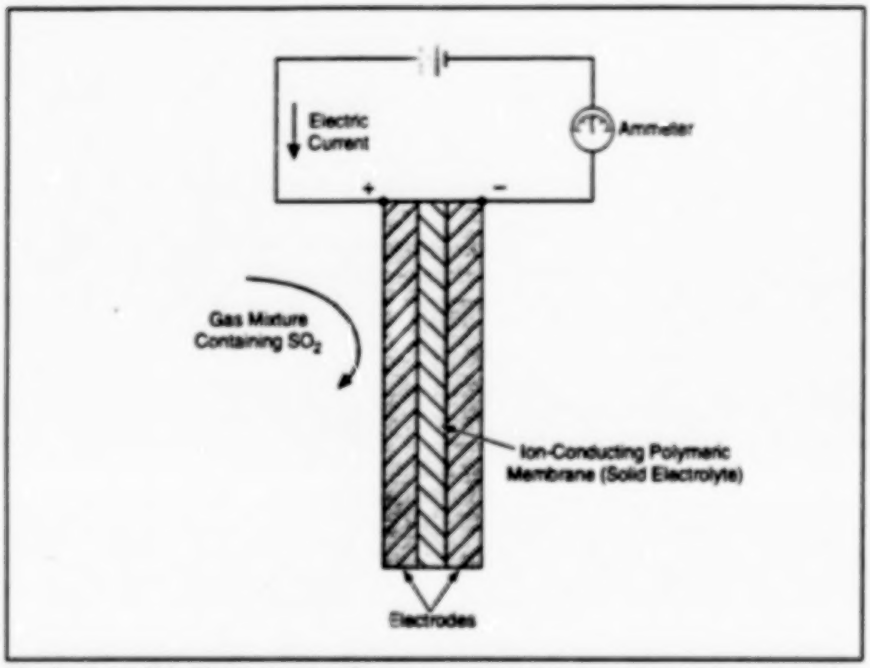
This work was done by Randall L. Vander Wal of NYMA, Inc., for **Lewis Research Center**. *Further information is contained in a TSP [see page 1].*

Inquiries concerning rights for the commercial use of this invention should be addressed to NASA Lewis Research Center, Commercial Technology Office, Attn: Tech Brief Patent Status, Mail Stop 7–3, 21000 Brookpark Road, Cleveland, Ohio 44135. Refer to LEW-16541.

Integrated Electrochemical Sulfur Dioxide Sensors

These sensors could be made small, lightweight, robust, and portable.

NASA's Jet Propulsion Laboratory, Pasadena, California



The Current in This Electrochemical Sensor is expected to be proportional to the concentration of SO_2 in the gas to which the positive electrode is exposed.

Integrated electrochemical sensors are being developed for use in measuring concentrations of sulfur dioxide in gas mixtures. These sensors are based on the electrochemical oxidation of SO_2 and measurement of the resulting electric current. Conceived for sensing SO_2 in volcanic gases, sensors of this type could also be used to monitor SO_2 in ambient air and in gases emitted during such industrial operations as metallurgical processing, refining of petroleum, and burning of coal.

Concentrations of SO_2 can be measured by mass spectrometers, but these instruments are too power hungry, heavy, and bulky to be portable, and their response times are too long for taking repetitive measurements in unsafe locations. The developmental sensors are inherently simple and fast-responding and could be made small, lightweight, and robust for incorporation into portable instruments that could be operated in industrial and remote natural settings.

A sensor of this type includes an integrated catalytic-electrode/ion-conducting-membrane/catalytic-electrode sandwich structure (see figure). The membrane is made of a proton-conducting polymer (for example, Nafion 117 or equivalent). The catalytic electrodes are made of porous carbon (graphite-based) paper substrates coated with catalysts in the form of platinum or platinum alloy powders. The electrodes on opposite sides of the membrane can be identical or different with respect to catalysts and treatments of the porous substrates. Such electrode/membrane/electrode sandwiches and techniques for fabricating them have been described in a number of previous articles in *NASA Tech Briefs*.

In operation, a dc potential is applied between the electrodes while the positive electrode is exposed to a gas mixture that contains SO_2. At the positive electrode, SO_2 in the presence of H_2O is oxidized to sulfate ions, with production of hydrogen ions, in the following chemical reaction:

$$SO_2 + 2H_2O \rightarrow SO_4^{2-} + 4H^+ + 2e^-$$

The hydrogen ions are conducted through the membrane to the negative electrode. Upon arrival at the negative electrode, the hydrogen ions react as follows:

$$2H^+ + 2e^- \rightarrow H_2$$

The current of hydrogen ions through the membrane gives rise to a measurable electric current in the wires connecting the electrodes to the source of applied potential. For a given fixed applied potential, the current is expected to be proportional to the concentration of SO_2 in the gas in contact with the positive electrode.

The use of noble-metal catalysts and graphite-based substrates makes the electrodes resistant to chemical degradation. The Nafion 117 or equivalent membrane material is a sulfonic acid-based polymer that also resists chemical degradation.

An experimental sensor was made from a conditioned Nafion membrane and electrodes comprising porous carbon paper catalyzed with platinum black. The electrodes were bonded to the membrane. The resulting sandwich was mounted between two glass flanges with electrical leads attached to the electrodes. The active sensor area was a square about 1 in. (about 2.5 cm) on each side. In tests, potential in the range of 1 to 2 V was applied and currents were measured with and without exposure to SO_2. Current responses on exposure to SO_2 were significant, and the response time was about 1 s. Further studies to quantify responses and sensitivity to operating variables were under way at the time of reporting the information for this article.

This work was done by Sekharipuram Narayanan and Santosh Srivastava of Caltech for **NASA's Jet Propulsion Laboratory**. *Further information is contained in a TSP [see page 1].*
NPO-20290

In Situ Chemical Analysis via Acoustic-Emission Spectra

Small piezoelectric sensors coated with reactive materials would provide data on chemical compositions.

NASA's Jet Propulsion Laboratory, Pasadena, California

A method of *in situ* chemical analysis by use of small, simple, robust sensors has been proposed. The basis for the proposal is the discovery that chemical reactions emit acoustic waves, and that characteristic frequency spectra are associated with specific reactions. The acoustic frequencies of interest range from about 0.1 to several megahertz. If a newly recorded acoustic spectrum were to match a previously recorded spectrum of a known chemical reaction, then the newly recorded spectrum would be deemed to indicate the presence of that reaction. The amplitude of a spectrum would be taken as an indication of the rate of the corresponding reaction.

A chemical-analysis instrument based on this concept would include an array of miniature piezoelectric acoustic sensors, each with a typical area of no more than a fraction of a square millimeter. The sensors would be able to withstand accelerations up to about 10^5 times that of normal Earth gravitation (about 10^6 m/s^2).

The instrument would include circuitry for flash analog-to-digital conversion of the sensor outputs, plus a moderately powerful digital data processor that would Fourier-analyze the digitized sensor outputs to obtain acoustic spectra. The instrument would also include electronic circuitry for (1) matching the newly acquired spectra with previously recorded spectra of known reactions and/or (2) recording and/or transmitting the newly acquired spectra for further processing by a computer to find matches to known spectra. The durations of typical chemical reactions of interest range from tens of seconds to hours; on this time scale, there would be no difficulty in time-multiplexing readouts from multiple sensors.

In the original proposed application, such an instrument would be used to find the chemical compositions of gases and dust in the Martian atmosphere, soil, and/or rocks. A similar terrestrial use would be monitoring gaseous, liquid, and solid pollutants in the field. For this purpose, the piezoelectric transducers would be coated with materials that engage in known chemical reactions with the pollutants or other substances of interest. Coatings could include adhesives to assist in collection of dust (and/or magnets to assist in collection of magnetic dust). Alternatively or in addition, reactive liquids could be injected into reaction sites at analysis time. Because the sensors would have low thermal masses, heating the sensors to reaction temperatures (if necessary) would consume little power — no more than milliwatts at the highest temperatures likely to be needed.

This work was done by Frank Hartley of Caltech for **NASA's Jet Propulsion Laboratory**. *Further information is contained in a TSP [see page 1].*
NPO-20222

Electrostrictive Thermal Break Between Superfluid Reservoirs

Superfluid in a connecting capillary would be rendered normal by electrostriction.

NASA's Jet Propulsion Laboratory, Pasadena, California

A proposed technique would make it possible to maintain two reservoirs of superfluid helium at the same pressure but at different temperatures. Heretofore, a fountain effect (described below) has made this impossible. The proposed technique could be useful for low-temperature experimentation and for the general processing of liquid helium.

Liquid helium becomes a superfluid when cooled below a temperature of 2.177 K. One of the characteristics of a superfluid is nearly infinite thermal conductivity. Thus, if two reservoirs containing superfluid helium are put in fluid communication to equalize their pressures, thermal conduction through the connecting fluid equalizes their temperatures. Even a connection as narrow as a capillary tube acts as a thermal short circuit.

One way to obtain a temperature difference between the two reservoirs is to make the fluid connection through a porous material (e.g., a ceramic). However, such a temperature difference is accompanied by a pressure difference; this is the phenomenon known as the fountain effect.

According to the proposal, the two reservoirs would be connected via an electrically conductive capillary tube, part of the interior of which would be occupied by an electrically insulated wire. A high voltage would be applied between the wire and the capillary tube. The resulting high electric field inside the tube would cause electrostriction in the fluid, so that the pressure in the capillary tube would increase. The increase in pressure would depress the superfluid-transition temperature, causing the fluid in the capillary tube to revert to a normal fluid. Because the fountain effect would not occur in the normal fluid, it would be possible to maintain a temperature difference between the opposite ends of the capillary tube.

The increase in pressure with electrostriction is given by

$$P = (\varepsilon_0/6)(d - 1)(d + 2)E^2,$$

where ε_0 is the vacuum permittivity, d (which equals 1.06) is the relative permittivity of liquid helium, and E is the electric field. A suitable device to implement the technique could be made from a wire of 0.003 in. (0.076 mm) outside diameter and a tube of 0.004 in. (0.102 mm) inside diameter. At the breakdown electric field of 10^8 V/m, it should be possible to depress the superfluid-transition temperature by 0.23 mK.

This work was done by Talso Chui and Yury Mukharsky of Caltech for **NASA's Jet Propulsion Laboratory**. *Further information is contained in a TSP [see page 1].*
NPO-20406

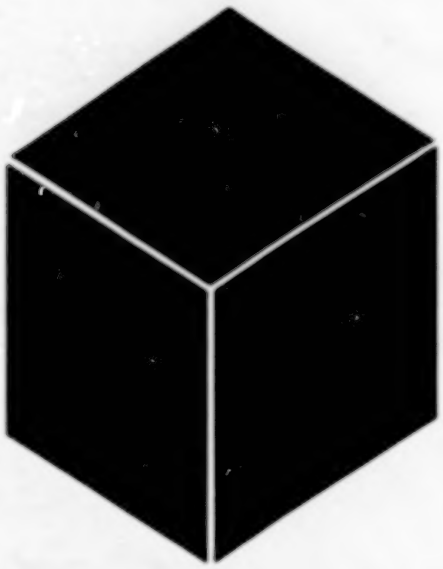
Books and Reports

Experiments on F v in a Model Compresso. Drum

A report discusses experiments on the flow of water along the interior of a transparent rotating cylindrical drum, the interior of which was partitioned into five cavities by disks with central holes and outer edges attached to the cylindrical drum wall. This water-flow model was designed to rovide insight into the flow in the com ressor drum cavity of an advanced, high-thrust engine. In the experiments, laser Doppler velocimetry was used to measure flow velocities. Laser-induced fluorescer (LIF) was used to measure tempera e fields and thereby also trace flow paths. LIF was also used to mea concentrations of salt in a fluoresce dye solution; such measurements were found to be useful for quantifying the mixing of a denser stream (the one containing the salt) with a stream of lesser density (the dye solution). Both types of LIF measure ments were found to be useful for investigating transient flow effects. Measureme.ts at mass-flow and tangential Reynolds numbers of 3×1 and 5.5×10^6, respectively, showed that the axial flow converges through a vena contracta that reduces the effective flow area by 31 percent. Fluid was found to be drawn into each cavity along the disk surfaces and to flow out between the disk surfaces in a forced vortex flow with no net flow entrained in the cavity.

This work was done by David G. N. Tse of Scientific Research Associates, Inc., for **Lewis Research Center**. *To obtain a copy of the report, "Experimental Simulation of Buoyancy Effect Using Two Liquids in Turbomachinery Components," see TSP's [page 1].*

Inquiries concerning rights for the commercial use of this invention should be addressed to NASA Lewis Research Center, Commercial Technology Office, Attn: Tech Brief Patent Status, Mail Stop 7–3, 21000 Brookpark Road, Cleveland, Ohio 44135. Refer to LEW-16449.



Materials

Hardware, Techniques, and Processes

29 Composite-Matrix Regenerators for Stirling Engines
30 Improved Alloy for Fabrication of Combustion Chambers by VPS
30 Etching Solution for Removal of Silver Plating From Polymers

BLANK PAGE

Composite-Matrix Regenerators for Stirling Engines

One can exploit the properties of composites to reduce thermal and flow losses.

Lewis Research Center, Cleveland, Ohio

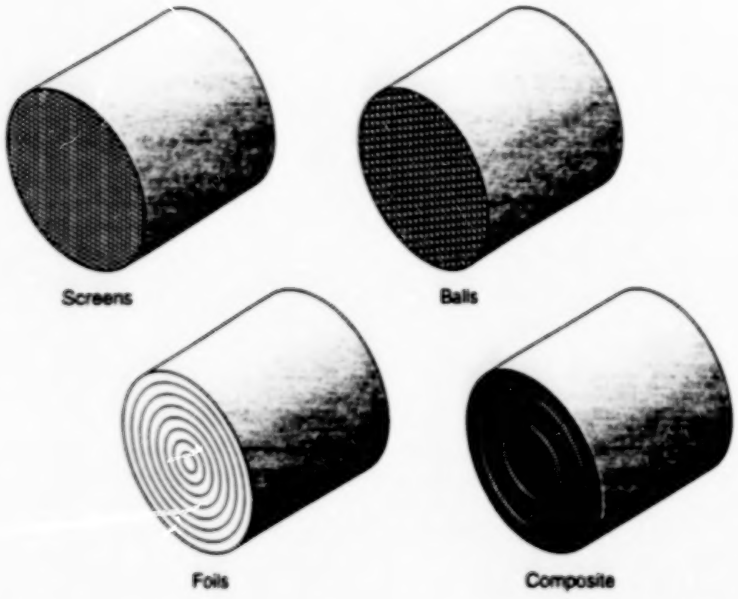


Figure 1. **A Composite-Matrix Regenerator** containing a matrix of radial carbon fibers offers advantages over current regenerators containing matrices of screens, balls, or foils.

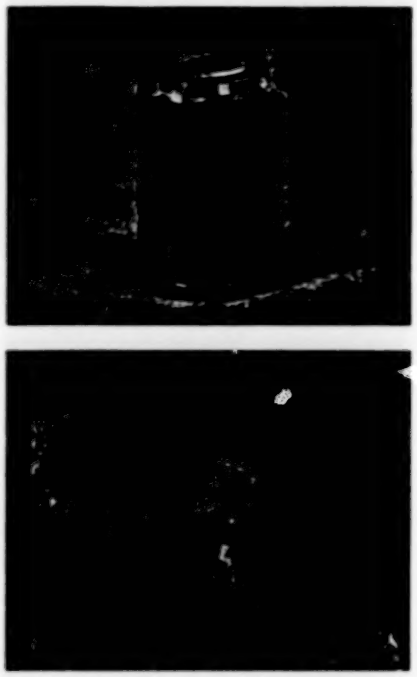


Figure 2. **This Prototype Composite-Matrix Regenerator is made of radially oriented carbon fibers bonded to an anisotropic carbon/carbon composite tube. Fabrication involved electrostatic flocking of the carbon fibers followed by rigidization (including thickening of the fibers) by chemical-vapor infiltration.**

A prototype Stirling-engine regenerator containing a matrix made of carbon-fiber-based composite materials has been developed. The concept underlying this development effort is one of exploiting the properties of composite materials (e.g., the anisotropy of thermal conductivity of carbon fibers and the tailorability of composite materials and structures) to reduce thermal and flow losses below those of previously developed regenerators containing metal matrices.

The regenerator in a Stirling engine is an internal heat exchanger for transferring heat between a working fluid and a flow-channel wall (which is also part of the regenerator). The fluid can be helium or another gas that has suitable thermodynamic properties and that does not react chemically with engine components. A typical regenerator is cylindrical in overall shape and includes one or more axial passage(s) containing a matrix — an open, thermally conductive structure with many flow paths and large surface area for transfer of heat to and from the working fluid. ("Matrix" as used here is meant to be distinguished from "matrix" as used elsewhere to designate the nonfibrous or nonparticulate component of a composite material. Hereafter in this article, the terms "regenerator matrix" and "matrix material" will be used to avoid ambiguity.) Stated somewhat differently, the matrix provides a thermal connection between the gas and the heat capacity of the wall.

Problems associated with making effective regenerators stem from limitations of materials of which they are made. Regenerator matrices are subjected to hot, oscillating gas flows and high temperature gradients. For high performance, a regenerator should be thermally insulating in the axial direction (along which a substantial thermal gradient can exist) and should exchange heat rapidly with the working fluid. The regenerator should contain minimum dead volume because dead volume reduces the engine compression ratio. The flow of gas through the regenerator matrix introduces drag and viscous losses, which should be minimized in order to maximize performance. Efforts at reducing some loss mechanisms tend to aggravate others.

Matrices in current regenerators have been made of various components, including steel wool, steel felt, stacked screens, packed balls, metal foils, and parallel plates. The matrix in a composite-matrix regenerator (CMR) could be made in any of a variety of composite materials and configurations; for example, regenerator matrices could comprise radially or circumferentially oriented thick fibers (see Figure 1). The fibers in the channels could be composites built up on thinner carbon-based fibers. The ends of the fibers would be embedded in cylindrical or otherwise-shaped axial-flow-channel walls.

Relative to current regenerators containing packed balls, felts, or stacked screens, CMRs containing fibers across axial-flow channels offer the potential advantage of greater heat-transfer effectiveness for a given flow friction. The high surface area of the fibers enhances gas/solid heat transfer, making it possible to obtain adequate performance from fewer, wider flow channels than one might otherwise need; this creates an opportunity to reduce costs because fewer, larger channels can be fabricated more easily. Other advantages of CMRs containing fibers crossing axial-flow channels, relative to current regenerators, include smaller pressure drops and smaller dead volumes.

The lengthwise thermal conductivities of graphitized carbon fibers range from about 300 to about 1,000 $Wm^{-1}K^{-1}$ — about 20 to 67 times the thermal conductivity of stainless steel. The transverse thermal conductivities of these fibers are only about 1/100 of their lengthwise conductivities. If

these fibers were combined with ... thermal-conductivity matrix material, the resulting composite materials exhibit high anisotropic thermal conduction. In principle, such fibers and matrix materials could be used to advantage in the regenerator in the following ways:

- The fibers could be used to conduct heat between the flowing gas and the flow-channel walls.
- The walls could be made of a composite material containing radially oriented fibers to utilize the thermal-conduction anisotropy to maximize radial conduction between the wall and the fibers in the channel while minimizing undesired axial conduction. Preferably, the matrix material in the wall would be one of high specific heat as well as low thermal conductivity.

Figure 2 shows a prototype CMR. A CMR of this type has survived limited endurance testing in a small Stirling engine, where it exhibited thermal performance among the best of a number of different regenerators that were tested.

This work was done by Timothy R. Knowles of Energy Science Laboratories, Inc., for **Lewis Research Center**. *Further information is contained in a TSP [see page 1].*

Inquiries concerning nights for the commercial use of this invention should be addressed to NASA Lewis Research Center, Commercial Technology Office, Attn: Tech Brief Patent Status, Mail Stop 7-3, 21000 Brookpark Road, Cleveland, Ohio 44135. Refer to LEW-16581.

Improved Alloy for Fabrication of Combustion Chambers by VPS

A shell has been fabricated by VPS, and experiments continue.

Marshall Space Flight Center, Alabama

Fabrication Process	Post-Fabrication Treatment	Density, g/cm³	Hardness, Rockwell B
VPS	None (Sample Tested As-Sprayed)	8.480	62.6
	Vacuum Anneal for 4 Hours at 1,750 °F (954 °C)	8.583	72.3
	Vacuum Anneal for 4 Hours at 1,750 °F (954 °C) and HIP for 1 Hour at Same Temperature	8.730	76.8
	HIP for 4 Hours at 1,750 °F (954 °C)	8.685	69.3
PM and Extrusion	None	8.660	70.9

Density and Hardness of Specimens of 88Cu/8Cr/4Nb were measured after various fabrication processes and treatments.

An alloy of 88Cu/8Cr/4Nb (numbers indicate atomic percentages) has been proposed for use in fabricating rocket-engine combustion chambers by vacuum plasma spraying (VPS). Relative to other techniques that could be used to fabricate rocket-engine combustion chambers, VPS is inexpensive. In VPS, a powder feedstock of the desired alloy becomes melted and deposited at high speed onto a substrate. Heretofore, those rocket-engine combustion chambers that have been fabricated by VPS have typically been made of the copper-based alloy NARloy-Z.

The 88Cu/8Cr/4Nb alloy was selected as a candidate to replace NARloy-Z because previous research had revealed that this alloy exhibits excellent high-temperature strength, resistance to creep, and low cycle fatigue behavior, all combined with exceptional thermal stability. Specimens of 88Cu/8Cr/4Nb fabricated by powder metallurgy (PM) had been found to exhibit better mechanical properties at a temperature of 1,200 °C than does NARloy-Z at 1,000 °C. The problem then became one of determining whether the superiority of PM 88Cu/8Cr/4Nb would carry over to VPS 88Cu/8Cr/4Nb.

In the first stage of an effort to investigate the properties of VPS 88Cu/8Cr/4Nb, VPS parameters to obtain an optimal deposit of this alloy on a cylindrical substrate were developed, then VPS was carried out to form a shell with a wall thickness of 0.5 in. (1.3 cm), and length of 6 in. (15 cm). Samples were machined from the 88Cu/8Cr/4Nb shell and analyzed for density and hardness. Some of the samples were further treated by vacuum annealing and/or hot isostatic pressing (HIP) prior to analysis.

The table presents the results of these analyses. For comparison, the table also presents the results of previous research on extruded PM 88Cu/8Cr/4Nb. The comparison reveals that the density and hardness of VPS 88Cu/8Cr/4Nb treated with vacuum annealing and HIP were greater than those of extruded PM 88Cu/8Cr/4Nb. These superior properties of the VPS 88Cu/8Cr/4Nb are expected to translate into superior tensile and low-cycle fatigue properties; experiments to verify this expectation had not been completed at the time of reporting the information for this article.

This work was done by Richard R. Holmes and Frank Zimmerman of **Marshall Space Flight Center** *and George P. Beason, Jr., and Timothy N. McKechnie of Plasma Processes, Inc. Further information is contained in a TSP [see page 1].*

MFS-26546

Etching Solution for Removal of Silver Plating From Polymers

Underlying polymeric materials are not attacked.

NASA's Jet Propulsion Laboratory, Pasadena, California

An etching solution has been developed for use in removal of silver plating from polymer-based (including composite-material) structural components, the surfaces of which are intended to serve as mirrors and waveguide structures. Such structures are often plated with aluminum, copper, and silver to impart the reflectivity and electrical conductivity required of mir-

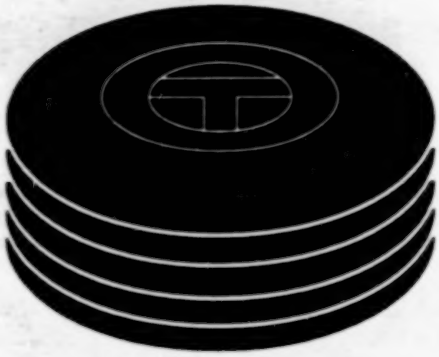
ror and waveguide surfaces. It is sometimes necessary to remove the plating in preparation for reworking mirror or waveguide hardware. The present etching solution satisfies a need for an effective, fast-acting, nonoxidizing plating-removal solution that does not destroy the underlying polymeric or composite material.

The present solution is a modified version of a previously developed and widely used copper chloride etching solution. During use of the previously developed solution, the plating is attacked by nonoxidizing chloride ions. The previously developed solution works well in removing most metals but is not suitable for use on silver because it leaves an insoluble silver chloride residue.

The present solution is a bright green liquid that consists of deionized water containing 5 percent by weight of cuprous chloride and 20 percent by weight (saturation concentration) of ammonium chloride. The addition of the ammonium ions prevents the formation of an insoluble silver chloride residue. Instead, ammonium ions form a complex soluble salt with silver; namely, silver ammonium chloride $[Ag(NH_3)_2Cl]$. A silver-plated polymeric or composite-material surface can be cleaned of all silver by immersion in this solution for as little time as 10 seconds. The solution also readily attacks most other metals — especially aluminum.

This work was done by Paul B. Willis of Caltech for **NASA's Jet Propulsion Laboratory**. *Further information is contained in a TSP [see page 1].*
NPO-20340

BLANK PAGE



Computer Programs

Physical Sciences

35 Program Simulates Performance of a Hybrid Automobile

BLANK PAGE

Computer Programs

These programs may be obtained from COSMIC. Please contact

COSMIC®
Computer Services Annex
University of Georgia
Athens, GA 30602
Telephone No. (404) 542-3265.

Physical Sciences

Program Simulates Performance of a Hybrid Automobile

Performance is estimated from vehicle parameters and operating conditions specified by the user.

The Hybrid Electric Vehicle Analysis (HEVA) computer program numerically simulates the performance of an automotive vehicle — especially a hybrid vehicle. A vehicle is said to be hybrid if (1) it contains an energy-storage device (a battery, flywheel, or ultra-capacitor) that is charged with energy from a heat engine that burns natural gas or another fuel and (2) the energy-storage device is part of a system that provides electricity to a traction motor for propulsion.

HEVA can mathematically model the performance of a conventional nonhybrid vehicle, which lacks an energy-storage device. It also accounts for energy recovered by regenerative brakes. For a given vehicle design and given operating conditions, HEVA calculates fuel economy and estimates itemized power flow, wheel and motor moments, and behavior of the energy-storage system. The algorithms in HEVA incorporate the assumption that the only direct source of motive power is an electric motor. HEVA cannot be used to analyze a hybrid vehicle with a parallel configuration, in which either an electric motor or a fuel-burning engine can propel the vehicle.

HEVA comprises a simulation subprogram and nine file-editor subprograms, which are used to modify the various input files. Each file-editor subprogram is dedicated to one of nine types of input files. The input data fall into the following categories:

- Operating conditions (velocity profile, road inclination, and environmental conditions);
- Some general vehicle parameters (including weight and aerodynamic characteristics);
- Engine parameters (including efficiency, power ratings, and fuel characteristics);
- Drive-train efficiency as a function of speed ratio;
- Torque supplied by the motor vs. motor speed ratio;
- Auxiliary power unit (APU) control parameters (adjusted APU power output vs. state of charge);
- Battery characteristics (open-circuit voltage and resistance vs. state of charge, rated voltage, and charge capacity in ampere-hours);
- Flywheel characteristics; and
- Capacitor characteristics (capacitance, efficiency, and maximum voltage).

HEVA is written in C++ for IBM-PC-compatible computers running Windows 95/NT. Executable code is provided. IBM Visual Age C++ is necessary for compiling any modifications of the code. The standard distribution medium for HEVA is a set of two 3.5-in. (8.89-mm), 1.44MB MS-DOS-format diskettes. An electronic copy of the documentation in HTML format is included on the distribution medium. HEVA was released to COSMIC in 1998.

This program was written by D. K. Stalnaker and L. Viterna of **Lewis Research Center**. *Further information is contained in a TSP [see page 1].*
LEW-16632

BLANK PAGE



Mechanics

Hardware, Techniques, and Processes

39 Flutterometer for Flight Testing

40 Model of Response of Pressure Sensor in Rarefied Flow

41 Improved Mufflers for General Aviation

BLANK PAGE

Flutterometer for Flight Testing

Flight data are used to predict unstable flight conditions.

Dryden Flight Research Center, Edwards, California

A flutterometer is being developed for use as a data-analysis tool for flight flutter testing. The tool is based on an on-line implementation of a robust flutter-analysis technique, called the "μ method," that was described in "Characterizing Worst-Case Flutter Margins From Flight Data" (DRC-97-03), *NASA Tech Briefs*, Vol. 21, No. 4 (April 1997), page 62.

Flight testing is performed to evaluate the characteristics of an aircraft and to determine a range of flight conditions, called a "flight envelope," in which an aircraft can be operated with safety. A particularly dangerous instability that one must avoid is flutter, which results from coupling between structural and aerodynamic forces. Flight flutter testing is flight testing for determining a safe flight envelope in which an aircraft will not exhibit a flutter instability.

In traditional methods of flight testing, one expands a flight envelope via a series of test points, using measurements (that is, sensor outputs) generated in response to some excitation. Such dynamical properties as damping are estimated from the measurement data, and trends are used to determine whether the envelope may be expanded further. These methods are inefficient, and to be able to use these methods, one must ensure that data points are closely spaced, inasmuch as the trends do not guarantee which increases in flight conditions may be safely considered. Also, flight flutter testing is potentially dangerous to the crew because an unexpected flutter instability (one not predicted from the trends) can occur during a transition to a new test point.

The μ method provides for computation of worst-case flight conditions for which flutter may occur, by consideration of errors and uncertainty in a mathematical model. The flutterometer uses flight data to identify errors and uncertainty in a model, so the resulting worst-case flutter margin is predicted by use of the μ method directly account for data that describe the aircraft (as distinguished from a mathematical model of the aircraft).

The flutterometer can reduce the risk and cost associated with flight flutter testing by predicting unstable flight conditions at a current test point in order to determine what increases in flight conditions may be safely considered for the next test point. The envelope expansion can proceed more rapidly, inasmuch as test points can be chosen on the basis of traditional, but unreliable, damping trends along with the additional information from flutterometer predictions.



Figure 1. The NASA F/A-18 Systems Research Aircraft, here shown high above Edwards Air Force Base, was mathematically modeled in a computational simulation to demonstrate the performance of the flutterometer.

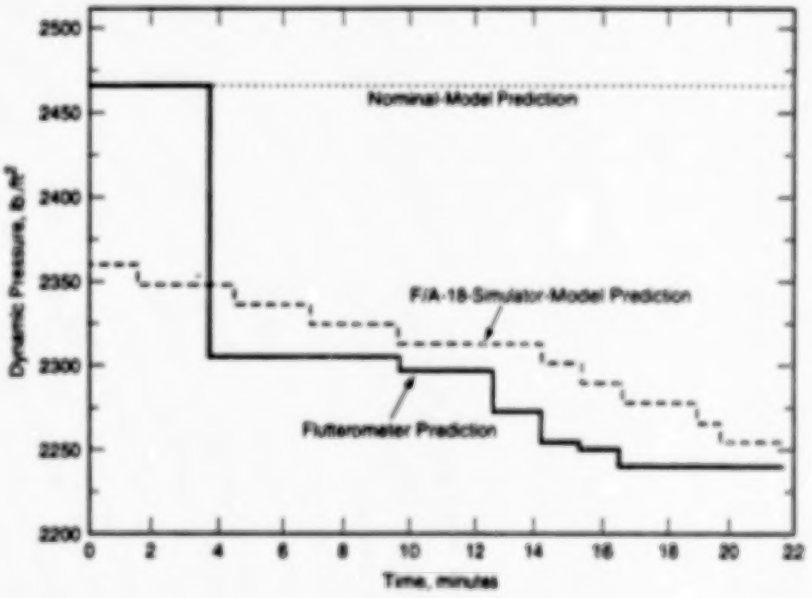


Figure 2. These Plots Show the Dynamic Pressures at which flutter was predicted to occur, as a functions of time, according to the flutterometer and to two mathematical models of the F/A-18 airplane.

A flight flutter test of the F/A-18 Systems Research Aircraft (see Figure 1), in which the envelope at mach 1.2 was expanded by decreasing altitude and increasing dynamic pressure, was simulated computationally to demonstrate the performance of the flutterometer. The

F/A-18 mathematical model used in the simulation provided for a representation of temporal variation of masses corresponding to consumption of fuel and for representation of measurements by wing-tip sensors. Another, nominal mathematical model of the F/A-18 airplane that includes 10-percent errors in structural stiffnesses and was formulated for constant mass corresponding to full fuel was used to predict unstable flight conditions for the simulated F/A-18.

Figure 2 shows the dynamic pressure at which flutter occurred as the simulation progressed. The dashed line represents the unstable flight conditions for the F/A-18 simulation; this line shows changes, even at constant-mach-number flight, because of the temporal variation of mass. The dotted line represents the traditional prediction, which was inaccurate inasmuch as it was based on the nominal model with no accounting for errors. The solid line represents the flutterometer prediction, which was computed by use of sensor data starting at 3 minutes (simulated time) after the beginning of the simulation to identify errors in the nominal model. These errors account for the unmodeled temporal variation of mass, so that the predicted worst-case flight conditions associated with flutter remain conservative to the true unstable conditions. The flutterometer could be used to determine safe test points for envelope expansion because the unstable flight conditions are predicted by use of data throughout the flight to account for unmodeled temporally varying dynamics.

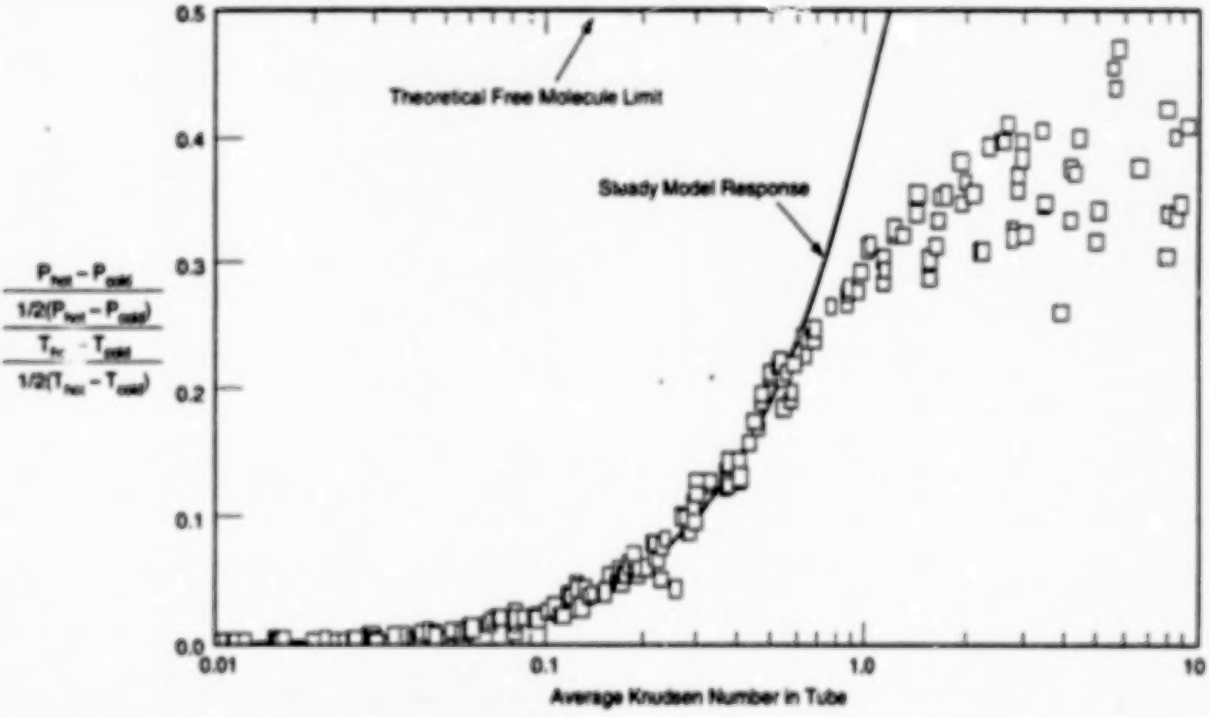
This work was done by Rick Lind and Martin Brenner of **Dryden Flight Research Center**. *Further information is contained in a TSP [see page 1].*

This invention is owned by NASA, and a patent application has been filed. Inquiries concerning nonexclusive or exclusive license for its commercial development should be addressed to the Patent Counsel, Dryden Flight Research Center [see page 1]. Refer to DRC-98-01.

Model of Response of Pressure Sensor in Rarefied Flow

Responses of pneumatic sensor systems can be evaluated over ranges of flow conditions.

Dryden Flight Research Center, Edwards, California



A Comparison of Steady-State Model Response to Measured Values of nondimensional steady response parameter for rarefied flow conditions shows that the model is valid for Knudsen numbers up to about 0.6 and is valid for most of the slip-flow regime.

A mathematical model represents the dynamic response of a pressure sensor that (a) comprises a transducer connected to a pressure-sensing port via a pneumatic tube and (b) is operated under flow conditions like those expected to be encountered on advanced hypersonic aerospace vehicles operating at high altitudes. The model is applicable to both continuum and rarefied flows, including flows accompanied by large gradients of temperature.

Heretofore, the influences of rarefied-flow phenomena on the responses of such a pressure sensor were not well understood. At the presence of hypersonic flow, not only are measurements affected by nominal spectral distortion and acoustical resonance, but in addition, a large temperature gradient induced by boundary-layer heating can induce a molecular transpiration effect, in which gas molecules adjacent to the tube wall creep from the cold end of the tube to the hot end. Furthermore, at low pressure typical of operation at very high altitude, the gas in the tube becomes so rarefied that the flow slips at the tube wall. The present mathematical model was developed to enable evaluation of the dynamic response (the frequency response) under these flow conditions.

The model was derived from the equations of energy, continuity, momentum, and state. Effects of rarefied flow are represented by letting fluid elements slip at the tube wall; this is opposed to the classical "no-slip" condition used in continuum flow mechanics. For flows characterized by values of the Knudsen number between 0.01 and 1.0, molecular and continuum flow effects are important. Under these conditions, free-stream flow away from the wall boundary is identical to continuum flow; however, at the wall, the fluid elements do not stick to wall as they would in continuum flow. Instead, fluid elements slip along the wall — hence the name "slip-flow" regime.

Under slip-flow conditions, the fluid velocity at the wall boundary can be decomposed into two parts: the slip velocity and the thermomolecular "creep" velocity. The slip velocity is proportional to the shear stress at the wall and is a result of reduced viscosity in a rarified fluid. The creep velocity is proportional to the longitudinal temperature gradient and inversely proportional to the local pressure. Kinetic theory predicts that gas molecules originating in the hotter region of the tube — having kinetic energies greater than those of molecules originating from the colder region — recoil more strongly than do the gas molecules from the colder region. As a result, the gas acquires a tangential momentum from the colder toward the hotter region. This net momentum gain causes the gas molecules at the wall to creep from the cold to the hot end of the tube.

To balance this creep, gas molecules in the center of the tube must migrate toward the colder end of the tube. The result of this "opposing flow equilibrium" is the establishment of a static pressure gradient such that cold region of the tube reads lower than the hot region and there is no net cross-sectional flow in the tube. At the wall boundary, the velocity is the sum of the slip and creep velocities. Other than this modification, the classical equations of fluid motion apply in this flow regime.

The equations of motion are linearized by use of small perturbations. The energy equation is decoupled from the momentum and continuity equations, assuming that the longitudinal wave expansion process within the tube is polytropic; that is, behaves according to a simple energy submodel that relates pressure, temperature, and density. The assumption of polytropic flow makes it possible to decouple the energy equation from the equations of momentum and continuity, without loss of generality. The boundary-value equations are radially averaged and solved with the help of the assumption that gas properties remain constant along the length of the tube. The resulting fundamental solution is used as a building block for complex situations in which fluid properties and tubing geometries vary longitudinally. The problem is solved recursively, starting at the transducer end and working toward the surface end of the tube. Using recursive formulas, solutions for arbitrary geometries and longitudinal temperature profiles are constructed.

The steady-state behavior of the model is analyzed by applying the final-value theorem to the recursive equation. The resulting expression is nondimensionalized and written as a function of the Knudsen number. Since it is extremely difficult to conduct controlled dynamic experiments under rarefied-flow conditions, the steady-state analysis is extremely important because it is the only feasible means of evaluating the range of validity of the slip-flow assumptions used in deriving the model.

Steady-state-response tests were performed under rarefied-flow conditions to verify the slip-flow assumptions used in deriving the boundary-value equations, and to establish a regime of validity for the model; the results (see figure) showed that the model is valid for Knudsen numbers up to about 0.6, and is valid for most of the slip-flow regime.

The model contributes to understanding of flow behavior at the limits of the continuum flow regime. It will enable instrumentation designers to evaluate the responses of pneumatic systems over a wide range of flow conditions in a general and unified way, without having to resort to *ad hoc* or special-case models. Potential nonaerospace applications of the model include prediction of the behaviors of fluids in micromachined systems, wherein the mean free paths of the working fluids are of the order of channel widths; and prediction of flows of highly viscous fluids for which Knudsen numbers can be sizeable under non-rarefied-flow conditions.

This work was done by Stephen A. Whitmore of **Dryden Flight Research Center** *and Brian Petersen of the University of California, Los Angeles. Further information is contained in a TSP [see page 1].*

DRC-95-34

Improved Mufflers for General Aviation

SiC foam serves as an absorber in a dissipative/reactive noise-suppression scheme.

Lewis Research Center, Cleveland, Ohio

Innovative designs of mufflers for engines of small airplanes have been investigated in an effort to satisfy conflicting demands to maximize the reduction of exhaust noise while minimizing back pressure, size, and weight. Automotive-type muffler designs are not suitable for this purpose because they entail excessive back pressures, sizes, and weights.

The investigation involved identification of key legal and technological issues in the silencing of general-aviation aircraft; development of a baseline theoretical approach to the design and optimization of aircraft engine exhaust systems; and evaluation of conceptual innovative designs of muffler and exhaust systems with dissipative, resistive, and reactive muffler components. The innovative designs call for the use of silicon carbide foam as a broadband absorber material in combination with reactive components; specifically, the designs feature variously sized and shaped expansion chambers with acoustic liners or flow-through baffles.

In experiments, acoustical impedances, resistances to flow, and other relevant properties of absorbers were measured and compared with theoretical predictions to determine such empirical parameters as structural factors. Noise characteristics of commercial aircraft engines were measured and compared with predicted values used in designing mufflers. Then prototypes of 17 different innovative muffler designs were fabricated, and several commercial aircraft engines were tested alternately with stock mufflers and with some of the prototypes to measure acoustic insertion losses as functions of frequency.

It was demonstrated that engine noise dominates overall aircraft noise for engines of less than 250 horsepower (power less than about 190 kW), and that mufflers can be beneficial toward

reducing aircraft noise. Final flightweight designs ha[illegible] not been developed at the time of rep[illegible]ng information for this article. Howe[illegible], it was de[illegible]rmined that because of the low frequencies of sounds generated by engines of the type in question, dissipative/reactive muffler designs like those investigated will be necessary for satisfying the noise, size, weight, [illegible] performance requirements of gener[illegible]ition. An additional advantage of th[illegible] muffler designs is that they are also [illegible] suitable for incorporation of catalyt[illegible]converters to redu[illegible]e chemical as well as noise pollution.

This work was done by [illegible]*drew J. Sherman, Sangvavann Heng, and Edwin P. Stankiewicz of Ultramet for* **Lewis Research Center**. *Further information is contained in a TSP [see page 1].*

Inquiries concerning rights for the commercial use of this invention should be addressed to NASA Lewis Research Center, Commercial Technology Office, Attn: Tech Brief Patent Status, Mail Stop 7-3, 21000 Brookpark Road, Cleveland, Ohio 44135. Refer to LEW-16324.



Machinery

Books and Reports

45 Performance of an Arc-Jet Thruster

BLANK PAGE

Books and Reports

Performance of an Arc-Jet Thruster

A report discusses the design and testing of a laboratory-model arc-jet thruster designed to operate at a nominal power level of 300 W. This thruster is an intermediate product of continuing efforts to develop smaller, lower-power, higher-specific-impulse thrusters for use in a forthcoming generation of small communication and scientific satellites. The thruster features a modular design, with a nozzle geometry chosen to promote supersonic-arc attachment. During tests, the thruster was operated at power levels from 200 to 400 W, using an improvised power supply and propellant-gas mixtures of hydrogen and nitrogen in proportions equal to those of hydrazine and ammonia. The performance of the thruster was found to depend strongly on the propellant-flow rate. Performance loss associated with viscosity in the nozzle was believed to increase with decreasing flow rate. Anode losses were essentially constant over the range of mass-flow rates used in the tests. The performance for the ammonialike gas mixture exceeded that for the hydrazinelike mixture; at a power of 300 W, the specific impulse and efficiency for the ammonialike mixture were 410 s and 0.34, respectively, while those for the hydrazinelike mixture were 370 s and 0.27, respectively.

This work was done by John M. Sankovic of **Lewis Research Center** *and David T. Jacobson of The Ohio State University. To obtain a copy of the report, "Performance of a Miniaturized Arcjet," see TSP's [page 1].*

Inquiries concerning rights for the commercial use of this invention should be addressed to NASA Lewis Research Center, Commercial Technology Office, Attn: Tech Brief Patent Status, Mail Stop 7-3, 21000 Brookpark Road, Cleveland, Ohio 44135. Refer to LEW-16503.

BLANK PAGE



Mathematics and Information Sciences

Hardware, Techniques, and Processes

49 Processing ScanSAR Data Using a Chirp z-Transform

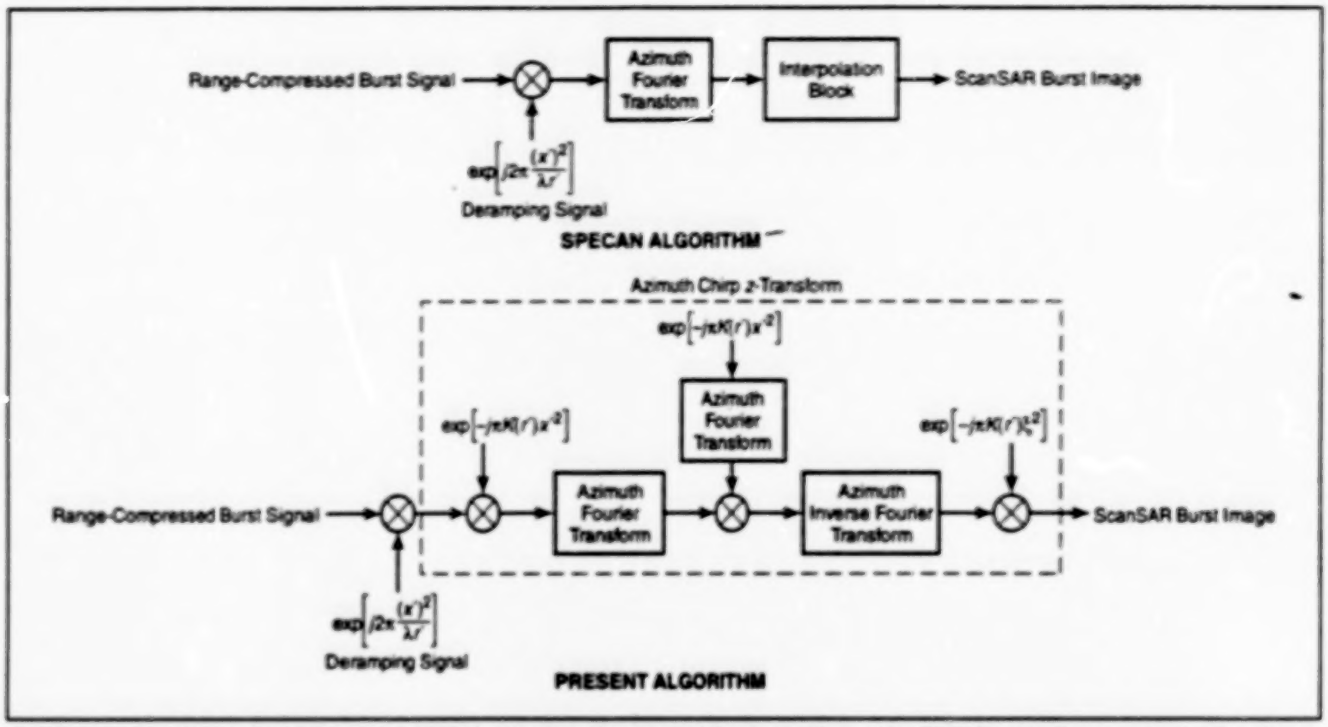
50 The *SPEEDES Qheap*: A Priority-Queue Data Structure

BLANK PAGE

Processing ScanSAR Data Using a Chirp z-Transform

A phase-preserving algorithm generates images with selectable constant azimuthal pixel length.

NASA's Jet Propulsion Laboratory, Pasadena, California



The Present Algorithm Is Derived from the SPECAN Algorithm. The standard Fourier transform of the SPECAN algorithm is replaced with a chirp *z*-transform, the kernel of which includes the range-dependent correction (scaling) factor $K(r') = r'_0/r'$, where r' is a range variable and r'_0 is a fixed range computed from the desired azimuthal pixel length. Regarding the other algebraic symbols: x' is an azimuthal coordinate, λ is the wavelength of the radar signal, and ξ is an azimuthal spatial frequency often interpreted in terms of Doppler frequency.

An algorithm that processes bursts of data generated by scan-mode synthetic-aperture radar (scanSAR) offers some advantages over older scanSAR algorithms. With relatively high computational efficiency, the algorithm can shift and scale the position along the flight track, preserve the phase of the radar signal, and provide for immediate formation of interferograms from two radar images.

Conventional practice in synthetic-aperture radar (SAR) involves the use of either the scan mode or the strip mode. The most commonly used mode is the strip mode, in which the radar antenna is pointed in a fixed direction with respect to the flight track and the illumination footprint covers a strip on the ground as the radar system moves along the flight track. The mapping swath is arbitrarily long in the azimuth (along-track) direction; as a result, the finest achievable resolution in azimuth (the along-track coordinate) is independent of range (radar/target distance) and equals half the along-track dimension of the antenna. High range resolution is obtained by use of either very short pulses or properly coded signals. The length of the range swath is limited by the pulse-repetition interval; in some applications, this can be undesirable.

In the scan mode, the radar beam is periodically stepped in range to neighboring swaths, which are denoted subswaths for scanSAR purposes. This stepping increases the length of the range swath, but exerts the undesirable effect of decreasing along-track resolution because the stepping prevents the collection of the return from a target along the full along-track synthetic antenna aperture length dimension of the synthetic aperture. The term "burst" is used to characterize both (1) the interval during which the radar beam illuminates a given subswath and (2) the data obtained from the subswath.

ScanSAR data could be processed following a standard range/Doppler approach that includes, among other things, the use of Fourier transforms for efficient frequency-domain implementation of convolutions. However, for reasons too complex to discuss within the limits of this article, this approach entails large zero-padding of burst data in preparation for azimuth compression, and this padding makes for computational inefficiency. An alternative approach is implemented by a very efficient algorithm called "SPECAN," in which azimuth focusing is accomplished in a process that involves a phase-multiplication operation called "deramping," followed by a Fourier-transform step. This process involves the original burst data with either no zero padding or very limited padding to the nearest power of 2 for a typical discrete-Fourier-transform code. Strictly speaking, the SPECAN algorithm does not compensate for range migration, but partly as a consequence of the shortness of bursts, the range-migration effects in most scanSAR applications are small enough that one can ignore them for practical purposes.

The present algorithm is an extended version of the SPECAN algorithm (see figure). One relevant characteristic of the SPECAN algorithm is the need for range-dependent scaling of the along-track pixel dimension. This scaling is accomplished in a post-processing interpolation step that can degrade either computational efficiency or accuracy, depending on the length of the interpolation kernel. In the present algorithm, the need for the scaling and post-processing interpolation is eliminated by replacing the standard Fourier transform of the SPECAN algorithm with a chirp *z*-transform, the kernel of which includes a range-dependent correction (scaling) factor. The chirp *z*-

transfo[rm] [c]an be computed by use of fast-F[ourier] transform software, without need[ing] [z]ero-padding; however, the prese[nt] [a]lgorithm is somewhat less efficient [t]han the SPECAN algorithm is because the chirp z-transform involves a convolution rather than a simple Fourier tr[ans]form.

The present algorithm is fully [p]hase-preserving [a]nd retains the relati[ve] simplicity and mod[est] of the computation[al] efficiency of the SPECAN algorithm. How[ever], unlike the SPECAN algorithm, the present algorithm automatically generates images with constant azimuthal pixel length, without interpolation; moreover, the azimuthal pixel length can be chosen to suit the application at hand.

This work was done by Riccardo Lanari, Scott Hensley, and Paul Rosen of Caltech for **NASA's Jet Propulsion Laboratory**. *Further information is contained in a TSP [see page 1].*

NPO-20389

The *SPEEDES Qheap*: A Priority-Queue Data Structure

This construct outperforms other data structures.

NASA's Jet Propulsion Laboratory, Pasadena California

The Synchronous Parallel Environment for Emulation and D[iscre]te-Event Simulation (SPEEDES) is [being] using a new general-purpose priority queue data structure called the *SPEEDES Qheap* for managing its set of pending events in ascending time order. Empirical studies have shown this data structure to outperform more traditional priority queue data structures for large numbers of elements without breaking down.

Two operations are required of the *SPEEDES Qheap*: (1) *Insertion* of time-tagged events (time represents a priority of an event — low time means high priority) and (2) *Removal* of the event with the smallest time tag. These operations help SPEEDES preserve causality since events, which may generate future events, must always be processed in ascending time order. The *SPEEDES Qheap* is composed of two lists: (1) a temporary list denoted as Q_{temp} and (2) a primary list denoted as Q_{heap}.

Insertions are always accomplished in constant time by adding the inserted event to the bottom of Q_{temp}. The minimum time tag of Q_{temp} is always maintained. If the newly inserted event has a smaller time tag than the previous value, the minimum time-tag value is updated. Removal of events is more complicated. There are two cases.

Case 1:

If the event with the smallest time tag is in Q_{temp}, then Q_{temp} is sorted using a very fast merge-sort algorithm for linked lists. The event with the smallest time tag is removed from Q_{temp} and returned as the next event. The rest of Q_{temp} is Metasized into a single Metaitem that is inserted into Q_{heap}. Note that the newly formed metaitem is actually a sorted list of events. The time tag of the metaitem is defined as the time tag of the first event in its sorted list. If the number of metaitems in Q_{heap} ever grows larger than a specified value, S, then the metaitems in Q_{heap} are further metasized into a single metaitem so that the number of metaitems in Q_{heap} is reduced back to one. This helps keep Q_{heap} small enough so that straight insertion of metaitems remains efficient. Metaitems may contain lists of other metaitems, which can contain lists of other metaitems, etc. In this way, Q_{heap} is a recursively linked list data structure that adheres to the heap property.

Case 2:

The event with the smallest time tag is in Q_{heap}. This is more difficult since it is possible that the item removed from the top of Q_{heap} is actually a metaitem itself. If this is so, then the metaitem must be untangled by removing its top item, redefining the rest of the list of the metaitem as a new metaitem, making sure that Q_{heap} does not have more than S elements (if it does, then the elements in Q_{heap} are turned into a single metaitem and placed back into Q_{heap} as a single element), and then inserting this new metaitem back into Q_{heap}. The untangling procedure is repeated until a single event is obtained.

Because heaps are known to have worst-case $log_2(n)$ amortized behavior, this data structure should never break down. Also, because it is composed exclusively of linked lists, it should have very low overheads. There are no complicated rotation operations or arbitrary balancing heuristics to apply. This data structure does not require resizable arrays or modular arithmetic schemes either. The only (slightly) complicated part of the *SPEEDES Qheap* is the untangling procedure (which is actually very straight-forward). Because of its nice properties, the *SPEEDES Qheap* is highly recommended for general-event list management in discrete-event simulations and for other applications that require general-purpose priority queues. Provided below is a step-by-step procedure for implementing the *SPEEDES Qheap*.

SPEEDES Qheap Insertion

1. Place the event to be inserted at the end of the Q_{temp}.
2. Update T_{min} if this item has the smallest time tag out of all the items in Q_{temp}.

SPEEDES Qheap Removal

1. Check if T_{min} is less than the time tag of [the] next item in Q_{heap}. If so, perform steps a through f and then return. Otherwise, go on to step 2.
   a. Sort Q_{temp} and then set T_{min} to infinity.
   b. Remove the top element (this is what is returned as the next event) and call it *NextEvent*.
   c. Metasize the rest of the elements from Q_{temp} into a new metaitem called $Meta_{temp}$.
   d. Check if Q_{heap} already contains S elements. If it does, metasize all of its elements into a new metaitem and place it back into Q_{heap} as its only element.
   e. Insert $Meta_{temp}$ into Q_{heap}.
   f. Return *NextEvent*.
2. Remove the top item from Q_{heap} and call it *NextItem*. Then loop over steps a through e below until *NextItem* is not a metaitem.
   a. Check if *NextItem* is a metaitem. If not, then break out of the loop and return *NextItem* as the *NextEvent*. Otherwise, we know that *NextItem* is a metaitem which must be untangled in the steps b–e below.
   b. Remove the top element from *NextItem* and call it *NewItem*. *NextItem* now contains one less item. If *NextItem* has only a single element, then unmetasize it so that *NextItem* is a regular item.
   c. Check if Q_{heap} already contains S elements. If it does, metasize all of its elements into a new metaitem and place it back into Q_{heap} as its only element.
   d. Insert *NextItem* into Q_{heap}.
   e. Set *NextItem* = *NewItem* and then go back to a.

This work was done by Jeffrey S. Steinman of Caltech for **NASA's Jet Propulsion Laboratory**. *Further information is contained in a TSP [see page 1].*

NPO-20095



Life Sciences

Hardware, Techniques, and Processes

53 Imaging System Shows Ischemic Regions

53 Neutrophil-Screening Assay Using Two-Color Flow Cytometry

BLANK PAGE

Imaging System Shows Ischemic Regions

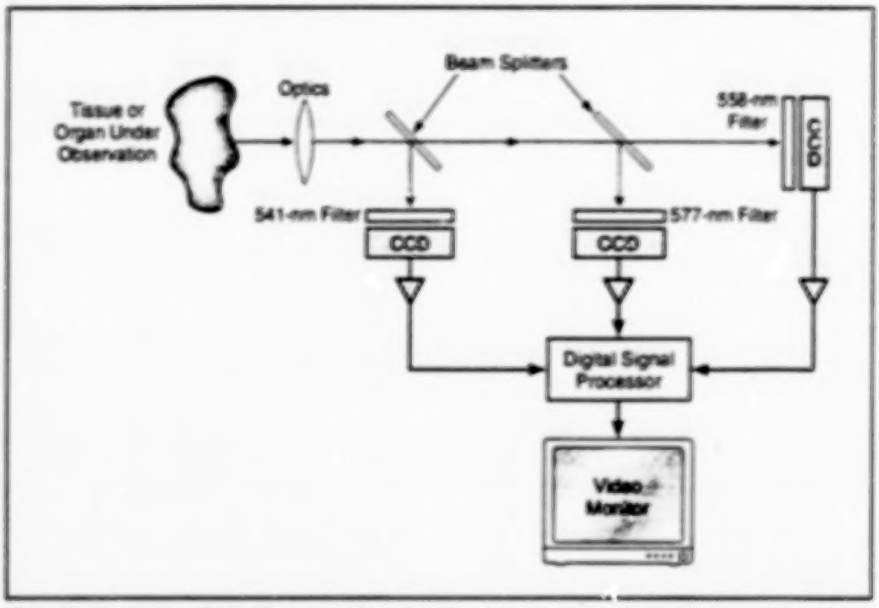
Real-time images help in monitoring and guiding treatments.

NASA's Jet Propulsion Laboratory, Pasadena, California

A noninvasive medical-imaging system produces false-color images that show regions of ischemia (reduced oxygenated blood flow) in organs and tissues. The system operates in real time, providing immediate guidance for surgery or other treatment. For example, the system can be used to identify tissues that should be removed in treating burns or in other surgical procedures.

The detection of ischemia involves the determination of the relative oxyhemoglobin and deoxyhemoglobin contents of blood in the affected organ or tissue. Heretofore, this has been done in nonimaging fashion by use of in-place monitors, such as pulse oximetry, which is not organ specific. The present noninvasive, real-time system is a multispectral imaging system that utilizes the spectral signatures of oxy- and deoxyhemoglobin.

The system (see figure) includes three charge-coupled-device (CCD) video cameras aimed at the same spot with the help of beam splitters. The light entering each camera passes through a narrow-bandpass filter at a unique wavelength. One possibility for wavelengths of the three filters is 541, 577, and 558 nm. These wavelengths were chosen because oxyhemoglobin has absorption peaks at 541 and 577 nm, while deoxyhemoglobin has an absorption peak at 558 nm. Another choice could include one of the isobestic points. Thus, as oxyhemoglobin is converted to deoxyhemoglobin, the 541-nm and 577-nm absorption peaks become depressed and the 558-nm absorption peak appears. Another choice may be 558 (deoxy peak), 569, and 586 (isobestic points).



This **Noninvasive, Real-Time Imaging System** utilizes three spectral absorption peaks characteristic of oxy- and deoxyhemoglobin.

The images acquired simultaneously at the three wavelengths can be processed and combined in such a way as to enhance the spectral contrast between deoxyhemoglobin and oxyhemoglobin. For this purpose, the video outputs of the three cameras are fed to a digital signal processor (DSP), which produces a false-color (red/green/blue) image of the organ or tissue that shows blood oxygen content. The DSP uses an algorithm derived from clinical data. This false-color image is displayed on a video monitor.

This work was done by Gregory H. Bearman, Thomas G. Chrien, and Michael L. Eastwood of Caltech for **NASA's Jet Propulsion Laboratory**. *Further information is contained in a TSP [see page 1].*

This invention is owned by NASA, and a patent application has been filed. Inquiries concerning nonexclusive or exclusive license for its commercial development should be addressed to the Patent Counsel, NASA Resident Office-JPL [see page 2 for address]. Refer to NPO-19569.

Neutrophil-Screening Assay Using Two-Color Flow Cytometry

This test can be performed rapidly and yields quantitative data.

Lyndon B. Johnson Space Center, Houston, Texas

An *in vitro* test that includes the use of two-color flow cytometry has been developed for use in screening of neutrophils for their ability to fight infections. Neutrophils constitute the first line of defense of the human body against infections. Neutrophils engulf invading bacteria in a process called "phagocytosis." The primary means by which they destroy the bacteria is the production of hydrogen peroxide and toxic oxygen radicals; this production is called "oxidative burst." Acquired defects in phagocytosis or oxidative burst can allow localized or generalized infections to develop. Such defects can be caused by toxins, drugs (including adrenocorticosteroids), and/or radiation. A rapid test that yields data on such defects could be helpful in choosing appropriate therapeutic measures prior to onset of overt clinical disease.

Most of the older *in vitro* tests developed for the same purpose require microscopy, are time-consuming, and involve much subjective judgement by highly trained technicians. One of the older tests is less subjective in that it yields quantitative data via an absorbance-spectrophotometric measurement of concentration of dye extracted from stained cells, but the disadvantage of this older test is that it requires a large amount of blood (as much as 10 mL). In contrast, the present test can be performed relatively quickly, requires a small amount of blood, and yields quantitative data.

In the present test, one uses stained cells of two species: the opportunistic pathogen *Candida albicans* and the intracellular pathogen *Listeria monocytogenes*. *Candida* is a common commensal that can cause serious disease if immunological

de[illegible] occur. *Listeria* is a catalase-prod[illegible] organism that is not killed after ph[illegible]ytosis if there is a defect in oxidative burst. (*Listeria* is used routinely in immunotoxicity testing.) Batches of *Candida* and *Listeria* organisms are stained with one of three fluorescent dyes (fluorescein isothiocyanate, CellTracker™, or Mitotracker™) for the purpose of testing for phagocytosis of those organisms. Neutrophils are stained with either of two other fluorescent dyes (dichlorofluorescein diacetate or hydroethidine) to detect oxidative burst with respect to those organisms.

In preparation for the test, the three types of cells are stained, then washed to remove excess dye. Neutrophils are mixed with cells of the other two types, and each mixture is incubated in a tube at an appropriate temperature. After an appropriate time (e.g., 1 hour), the incubation is stopped by putting the tubes on ice. A dilute suspension of cells in liquid is made from each mixture, and a jet of the liquid is made to cross a beam of light of wavelength 488 nm generated by an argon-ion laser in a flow cytometer. By use of photodetectors and band-pass filters in combination with a dichroic mirror, intensities of red and green fluorescence are measured, both in the forward- and perpendicular-scatter directions. These measurements are processed to determine the percentage of fluorescent neutrophils and the peak modal channel of fluorescence of the neutrophils. They are also used to generate a display of fluorescence intensities in a histogram or in a two-color contour plot.

This work was done by Duane L. Pierson of **Johnson Space Center** *and Raymond P. Stowe and Sanj K. Mishra of KRUG Life Sciences. Further information is contained in a TSP [see page 1].*

This invention is owned by NASA, and a patent application has been filed. Inquiries concerning nonexclusive or exclusive license for its commercial development should be addressed to the Patent Counsel, Johnson Space Center, (281) 483-0837. Refer to MSC-22654.

National Aeronautics and
Space Administration



55

END

02\09\99